Solar Phys (2019) 294:31
https://doi.org/10.1007/s11207-019-1416-8

Solar Terrestrial Relations Observatory (STEREO) Observations of Stream Interaction Regions in 2007 – 2016: Relationship with Heliospheric Current Sheets, Solar Cycle Variations, and Dual Observations

L.K. Jian[1] · J.G. Luhmann[2] · C.T. Russell[3,4] · A.B. Galvin[5,6]

Received: 14 November 2018 / Accepted: 14 February 2019 / Published online: 6 March 2019

Abstract We have conducted a survey of 575 slow-to-fast stream interaction regions (SIRs) using *Solar Terrestrial Relations Observatory* (STEREO) A and B data, analyzing their properties while extending a Level-3 data product through 2016. Among 518 pristine SIRs, 54% are associated with heliospheric current sheet (HCS) crossings, and 34% are without any HCS crossing. The other 12% of the SIRs often occur in association with magnetic sectors shorter than three days. The SIRs with HCS crossings have slightly slower speeds but higher maximum number densities, magnetic-field strengths, dynamic pressures, and total pressures than the SIRs without an HCS. The iron charge state is higher throughout the SIRs with an HCS than the SIRs without an HCS, by about 1/3 charge unit. In contrast with the comparable phases of Solar Cycle 23, slightly more SIRs and higher recurrence rates are observed in the years 2009 – 2016 of Cycle 24, with a lower HCS association rate, possibly attributed to persistent equatorial coronal holes and more pseudo-streamers in this recent cycle. The solar-wind speed, peak magnetic field, and peak pressures of SIRs are all lower in this cycle, but the weakening is less than for the comparable background solar-wind parameters. Before STEREO-B lost contact in October 2014, 151 SIR pairs were observed by the twin spacecraft. Of the dual observations, the maximum speed is the best correlated of the plasma parameters. We have obtained a sample of plasma-parameter differences analogous to those that would be observed by a mission at Lagrange points 4 or 5. By studying several cases with large discrepancies between the dual observations, we investigate the effects of

✉ L.K. Jian
lan.jian@nasa.gov

1 Heliophysics Science Division, NASA Goddard Space Flight Center, Greenbelt, MD 20771, USA

2 Space Science Laboratory, University of California, Berkeley, CA 94720, USA

3 Institute of Geophysics and Planetary Physics, University of California, Los Angeles, CA 90095, USA

4 Department of Earth, Planetary, and Space Sciences, University of California, Los Angeles, CA 90095, USA

5 Institute for the Study of Earth, Oceans, and Space, University of New Hampshire, Durham, NH 03824, USA

6 Department of Physics, University of New Hampshire, Durham, NH 03824, USA

HCS relative location, tilt of stream interface, and small transients on the SIR properties. To resolve the physical reasons for the variability of SIR structures, mesoscale multi-point observations and time-dependent solar-wind modeling are ultimately required.

Keywords Solar wind · STEREO mission · Stream interaction · Corotating interaction region · Solar Cycle · Shock

1. Introduction

The twin *Solar Terrestrial Relations Observatory* (STEREO) spacecraft were launched on 25 October 2006 from the Cape Canaveral Air Force Station in Florida. In early 2007, both spacecraft entered heliocentric orbits, orbiting with the Earth around the Sun in the ecliptic plane, one ahead of Earth called STEREO-A (STA), the other one trailing behind called STEREO-B (STB), drifting apart with increasing longitudinal separation from Earth of about 22° per year (Kaiser *et al.*, 2008). The STEREO mission has provided two vantage points for solar and solar-wind monitoring and enabled many joint science investigations with other missions.

When a spacecraft reaches the opposite side of the Sun from the Earth, the solar radio interference makes it impossible to communicate with the spacecraft from the Earth. The spacecraft needs to be placed into "safe mode" until it emerges on the other side (stereo-ssc.nascom.nasa.gov/solar_conjunction_science.shtml). On 1 October 2014, STEREO-B lost contact with the ground station during a rehearsal of the spacecraft reset. Although the communication with STB was regained for about one month (21 August 2016 – 22 September 2016), the spacecraft has been out of contact again since 23 September 2016 (stereo-ssc.nascom.nasa.gov/behind_status.shtml). There has been no science data from STB since 1 October 2014.

On the other hand, STEREO-A returned to normal operations in November 2015 after the solar conjunction, and solar-wind data are partially available in September 2014 – November 2015. Since STA and STB crossed paths on the far side of the Sun in 2015, they have been approaching the Earth from the opposite directions with their longitudinal separations from the Earth decreasing at the same rate of about 22° per year. At this writing, the STA and STB spacecraft are about 103° apart from the Earth, nearing the quadrature (90° separations).

The STEREO mission has operated during the deep Solar Minimum 23/24 and Solar Cycle 24, the weakest cycle in the Space Age, and probably the weakest cycle within a century, according to the sunspot record. Jian *et al.* (2018) found that fewer interplanetary coronal mass ejections (ICMEs) were observed by STEREO in contrast with a similar phase of the previous cycle. Herein we instead focus on the other type of large-scale solar-wind structures, the slow-to-fast stream interaction regions (SIRs). Like ICMEs, SIRs can produce geomagnetic storms, although they are usually only weak to moderate in strength. They also tell us about the connections between coronal and heliospheric structures, which are important for understanding space-weather responses, including ICME propagation.

An SIR is the compression region formed when a fast-wind stream overtakes a preceding slow-wind stream (*e.g.* Belcher and Davis, 1971). On the trailing part of the fast wind, a rarefaction region forms. The slow-to-fast SIRs are the same as the commonly known corotating interaction regions (CIRs) in nature. We use the generic term SIR introduced by Gosling *et al.* (2001), which is easy for describing mid-to-high latitude interaction regions

between the slow and fast wind. We consider SIRs that last more than one Carrington rotation ($\approx$27.3 days) to be CIRs (Jian *et al.*, 2006a). When the Sun is active, the source regions can change dramatically within one solar rotation; we would not necessarily observe the same SIR one Carrington rotation later. From the solar-cycle variation of the ratio of CIRs to SIRs, Jian, Russell, and Luhmann (2011) and Jian *et al.* (2013) estimated the stability of the solar-wind streams for quiet and active conditions.

In Section 2, we introduce the data set used and the identification criteria of SIRs and report some statistical results, including the speed-acceleration rate and shock-association rate. In Section 3, we compare the properties of SIRs associated with and without heliospheric current sheet (HCS) crossings, including histogram distributions of SIR parameters and superposed epoch analyses of iron charge-state distributions. In Section 4, we report the solar-cycle variations of SIRs and compare the similar phase of this solar cycle with the previous cycle. In Section 5, we survey the dual observations of SIRs by STA and STB, and study the variations of SIR parameters with spatial separations and demonstrate that some of the variability is caused by small transients, tilt of stream interface, and the change of the relative location with respect to the HCS. We finally summarize and discuss the results in Section 6.

2. Data Set and Identification Criteria

2.1. Data Set

To conduct the SIR survey for the STEREO mission, we use the one-minute magnetic-field and solar-wind-proton data from the *In situ Measurements of Particles and CME Transients* (IMPACT) Investigation (Luhmann *et al.*, 2008) and the *Plasma and Suprathermal Ion Composition* (PLASTIC) Investigation (Galvin *et al.*, 2008), respectively. Higher-cadence (0.125-second) magnetic-field data are used in the analysis of shocks and other small-scale structures. The 30-second suprathermal-electron data from IMPACT are used mainly for the identification of the HCS. The solar-wind plasma data from PLASTIC became available around March 2007. The magnetic-field and plasma data are unavailable or with reduced coverage from late August 2014 to middle November 2015, due to the solar conjunction. See Table 1 of Jian *et al.* (2018) for more details. Events appearing during the data gaps, or strongly masked by the data gaps, are not included in the survey. We calculate the event occurrence rates in 2007, 2014, and 2015, by normalizing by the available days.

Because STEREO α-particle data after 2011 are not generally available and the α-particle data available in 2007 – 2010 are of ten-minute cadence with about half of the time in data gaps, we approximate its density by 4% of the proton density and its temperature by four times the proton temperature in the calculation of total pressure [P_t], which is the sum of the plasma thermal pressure and magnetic pressure. These approximations have been verified using the available data in 2007 – 2010. As there are no thermal-electron data from STEREO, we assume charge neutrality and a constant electron temperature of 130,000 K (Jian *et al.*, 2006a, 2006b, and the references therein) to calculate P_t. With the lack of temperature-anisotropy data, we assume that the temperature is isotropic and use total pressure to approximate the total perpendicular pressure (Russell, Shinde, and Jian, 2005). All of the above assumptions were also used in the SIR survey of the *Wind* and *Advanced Composition Explorer* (ACE) data by Jian *et al.* (2006a) and Jian, Russell, and Luhmann (2011).

2.2. Identification Criteria

To identify the SIRs, we use the following set of criteria, as used previously by Jian *et al.* (2006a, 2008a, 2008b) and Jian, Russell, and Luhmann (2011): overall increase of solar-wind speed, pile-up of P_t with gradual declines at both sides (Gosling and Pizzo, 1999), a compression of magnetic field, first increase and then decrease of proton number density [N_p], increase of proton temperature [T_p], increase of proton specific entropy [S] defined as $\ln(T_p^{3/2}/N_p)$ (Neugebauer *et al.*, 2004), and deflection of solar-wind velocity. Not all of these features are necessarily present in each SIR, thus we generally require the presence of five features, one of which must be the overall speed increase, and also identify SIRs with careful consideration of the ambient solar wind such as nearby HCSs and ICMEs. In addition, for ambiguous events we check the coronal source regions after back-shifting the propagation time and the iron charge-state distribution to exclude the possible influence from CMEs. The boundaries of SIRs are delineated where the P_t emerges from and decays back to the background based on a consensus of the available plasma and magnetic-field signatures. A sharp change of P_t and/or other parameters, particularly a shock if it exists, is often a good separator of the SIR from the background.

The boundary separating the originally fast, tenuous, and kinetically hot solar wind from the slow, dense, and kinetically cold solar wind should be indicated by rapid density decrease and temperature increase. Gosling *et al.* (1978) found that such sharp boundaries exist in about 1/3 of SIRs observed at 1 AU in 1971 – 1974. From a 12-year SIR survey using *Wind* and ACE data, we see such simultaneous changes only in 21% of SIRs, given a temporal window of ten minutes (Jian, 2008). The corresponding thickness is about 2.4×10^5 km, which is six and four times larger than the thickness of the stream interface (SI) used by Gosling *et al.* (1978) and McComas *et al.* (1998), respectively. To define a stream interface uniformly, we choose the time when the P_t is maximized, because the forces pushing against its two sides should be equal (Jian *et al.*, 2005, 2006a).

As an example, Figure 1 displays dual observations of an SIR on 17 – 19 May 2007 from STA and STB. At both spacecraft, about six hours earlier than the SI, there is a clear HCS crossing from the toward (Sunward) sector to the away (anti-Sunward) sector, signaled by the changes of pitch-angle distribution of suprathermal electrons and the Parker-spiral angle. Coincident with the HCS at STA, there is a sharp drop of N_p and a prompt increase of T_p. Within the two hours before the HCS shaded in pink, the N_p is at least doubled and elevated to nearly 70 cm^{-3}; the magnetic field drops by more than a half, and plasma β (not shown) increases by one order of magnitude, suggesting this region is a heliospheric plasma sheet (HPS), *e.g.* Gosling *et al.* (1981), Bavassano, Woo, and Bruno (1997), Crooker *et al.* (2004a), and Winterhalter *et al.* (1994). STA observes multiple, brief field inversions (prompt large changes of the spiral angle) at the two sides of the HCS, more in the fast-wind side. These inversions are sometimes associated with magnetic-field dips and pitch-angle spectrogram vertical stripes, indicating an isotropic distribution of the suprathermal-electron flux, possibly attributed to interchange reconnection (*e.g.* Crooker *et al.*, 2004b; Owens, Crooker, and Lockwood, 2013). There are moderate temporary increases of T_p and S in four of the six field inversions near the HCS, all in the fast-wind side. The data coverage of α-particles is too sparse in this event to show any relation between the α-particle parameters and field inversions. Separated by 0.1 AU in radial distance and a few degrees in latitude and longitude, STB does not observe the HPS or field inversions, suggesting the mesoscale variability of the HPS.

The azimuthal-flow deflection from westward to eastward (blue curves in the third panels in Figure 1) at this SIR is observed by both spacecraft and is of similar scale. The meridional-flow deflection is slightly northward crossing the SI. Due to a small transient (cyan-shaded

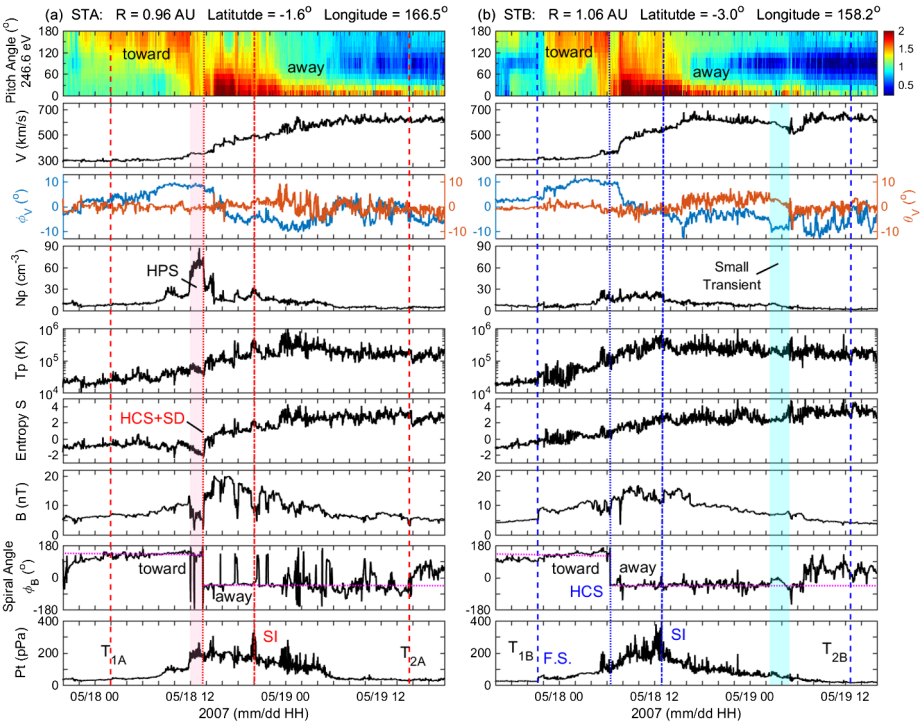

Figure 1 The SIR observed by (**a**) STA and (**b**) STB on 17 – 19 May 2007. The spacecraft locations in the heliographic inertial (HGI) coordinate (Fränz and Harper, 2002) are listed at the *top*. From *top* to *bottom*, the *panels* are the pitch-angle distribution of suprathermal-electron flux at 246.6 eV, solar-wind speed, azimuthal-flow angle [φ_V] defined as $\arctan 2(V_t, V_r)$ in *blue curve*, meridional-flow angles [θ_V] defined as $\text{asin}(V_n/V)$, proton number density, proton temperature, entropy, magnetic-field intensity, and the Parker-spiral angle of the magnetic field [φ_B] defined as $\arctan 2(B_t, B_r)$ (the *magenta-dotted lines* at 135° and −45° mark the nominal spiral angles for the toward and away sectors, respectively) and total pressure. In (**a**) at STA, the pair of *red-dashed lines* denotes the start and stop of SIR (T_{1A} and T_{2A}); the *pink-shaded region* marks the heliospheric plasma sheet (HPS); the *red-dotted line* indicates the HCS coincident with the sharp discontinuity (SD) of proton number density and temperature; and the *red-dash–dotted line* marks the SI uniformly defined at the peak of P_t. In (**b**) at STB, the pair of *blue-dashed lines* denotes the start and stop of SIR (T_{1B} and T_{2B}); there is a forward shock (FS) at the leading edge; the *blue-dotted line* indicates the HCS; the *blue-dash–dotted* line marks the SI, and the *cyan-shaded region* marks a small transient.

region in the right panels) at about 2:30 – 5:00 UT on 19 May, the solar-wind flow at STB drops and the direction angles around it differ noticeably from STA. Such a small transient is missed by STA. A forward shock is detected at the leading edge of the SIR at the STB, but no associated shock is observed by the STA, suggesting the SIR-driven shocks are still in development (*e.g.* Jian *et al.*, 2009). The propagation time from the STA to STB can be estimated using

$$t_B - t_A = (\varphi_B - \varphi_A)/\omega_{Sun} + (R_B - R_A)/V, \quad (1)$$

where φ denotes the spacecraft longitude, ω_{Sun} is the solar rotation angular speed, R is the heliocentric distance, and V is the solar-wind speed (*e.g.* van Hollebeke *et al.*, 1978; Richardson, Mazur, and Mason, 1998). Using the photospheric equatorial angular speed $\omega_{Sun} = 14.38° \,\text{day}^{-1}$ (Newton and Nunn, 1951) and the mean solar-wind speed of 482 $\text{km}\,\text{s}^{-1}$ within the SIR from STA observation, the calculated time difference from STA

to STB should be −0.218 day, *i.e.* −5.2 hours, close to the observed time difference of −3.6 hours for the middle time of the two SIRs.

2.3. SIR Survey and Statistical Results on Acceleration Rate and Shock Rate

In total, STA and STB observed 575 SIRs in 2007 – 2016, and the survey is provided to the public as a Level 3 product from the STEREO mission with multiple file formats at www-ssc.igpp.ucla.edu/forms/stereo/stereo_level_3.html, including one for the Space Physics Archive Search and Extract (SPASE: Roberts *et al.*, 2018), which is the uniform metadata for the Heliophysics Data Environment (hpde.gsfc.nasa.gov/index.html). About 50 (8.7%) of SIRs, although still meeting SIR criteria, are hybrid events combined with ICMEs, marked by an asterisk in the survey. In such hybrid cases, the remnant energetic particles trapped in ICME loops might serve as a seed population for SIR acceleration (*e.g.* Gómez-Herrero *et al.*, 2009). In a few SIRs, *e.g.* 10 – 13 May 2012 at STA, 22 – 24 March 2012, 28 – 29 April, and 19 – 21 September at STB, their fast speed is unusually slow (about 400 – 430 km s^{-1}), but the time profiles of N_p and T_p clearly show two different solar-wind streams interacting in each of those regions, sometimes with a sharp interface. It is interesting that these events tend to appear in 2012 – 2014 when the Sun is more active and the corona is more structured. Wang *et al.* (2012) suggested that pseudo-streamers would produce outflow that is intermediate between classical slow and fast solar wind. However, some of these SIRs are associated with an HCS crossing nearby. We mark such debatable SIRs using a question mark in the online survey at www-ssc.igpp.ucla.edu/forms/stereo/stereo_level_3.html, and there are seven such events, with one in the hybrid events. Their rare occurrence does not affect the SIR statistics in Section 4.

An SIR includes accelerated slow wind and decelerated fast wind. However, because there is often no clear boundary separating slow and fast wind, and because the speed-change rate usually does not vary much from the slow-wind portion to the fast-wind portion, we can use the average speed-change rate over an SIR to estimate the acceleration rate. Because the SIR does not necessarily end right at the end of the speed ramp and sometimes includes part of the unaffected fast wind, such as shown in Figure 1, the actual acceleration rate would be at times higher than from this calculation. For the 519 well-defined or pristine SIRs with available data, the acceleration rate ranges from 0.3 to 8.2 m s^{-2}. Figure 2 shows the scatter plots and correlations between the maxima of proton number density, magnetic-field magnitude, and total pressure *versus* the average acceleration rate across each SIR event. These parameters are generally positively correlated with the average acceleration rate, with the highest correlation coefficient being 0.6 for the peak total pressure [P_{tmax}].

More than 500 interplanetary shocks were analyzed in 2007 – 2016 using STEREO data. A catalog of shocks including the shock parameters and drivers are provided at www-ssc.igpp.ucla.edu/forms/stereo/stereo_level_3.html as well. Figure 3 displays the solar-cycle variations of the shock rates for forward shocks (blue bars), reverse shocks (green bars), and forward-reverse shock pairs (yellow bars) among all SIRs (second panel) and pristine SIRs (third panel). The forward-shock rate varies nearly in phase with sunspot activity while the reverse-shock rate does not have clear solar-cycle dependence. See more discussion in Section 4. Overall, about 33% of the 575 SIRs are associated with shocks, specifically about 19% with only forward shocks, 10% with only reverse shocks, and 4% with shock pairs. The partitions between forward and reverse shocks are similar to the results in Jian *et al.* (2006a). If we only consider the 519 pristine SIRs, the total shock rate decreases slightly to 30%, and the rates of only forward, reverse, and shock pairs are 16%, 10%, and 4%, respectively. The rate decrease mostly occurs for forward shocks, as compared in the second and

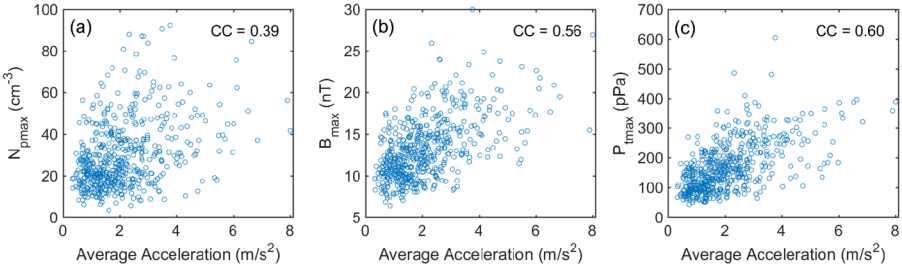

Figure 2 The scatter plots of SIR maximum parameters *versus* the average acceleration rate across each event for 519 pristine SIRs: (**a**) maximum proton number density *versus* average acceleration rate, (**b**) maximum magnetic-field strength *versus* average acceleration, (**c**) maximum total pressure *versus* average acceleration. The Pearson correlation coefficient (CC) is listed at the *top right corner* in each *panel*.

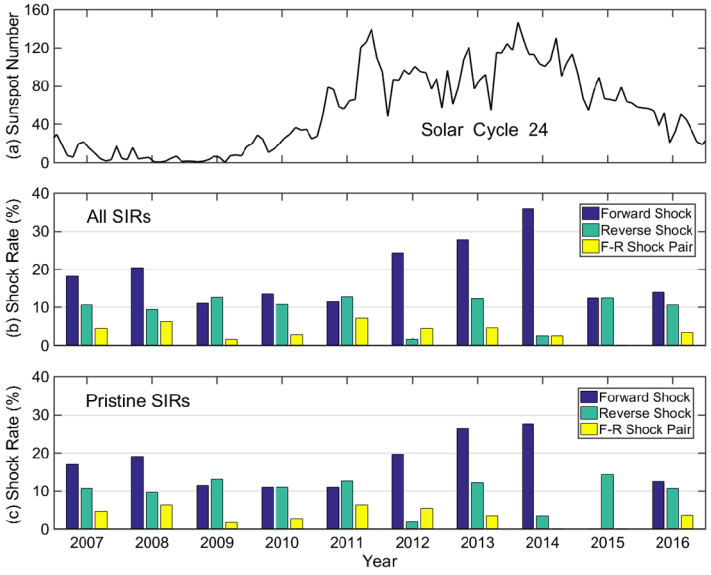

Figure 3 Solar-cycle variations of (**a**) monthly sunspot number, (**b**) shock rates for all SIRs, (**c**) shock rates for pristine SIRs in 2007 – 2016. *Blue bar* indicates the rate of only forward shock; *green bar* marks the rate of only reverse shock; and *yellow bar* indicates the rate of forward-reverse shock pair.

third panels of Figure 3. It is expected because hybrid events in which ICMEs interact with SIRs would often drive forward shocks. Some SIRs are associated with two forward shocks, for instance, SIRs on 8 – 10 July 2012, 29 – 31 December 2013, and 20 – 23 January 2014 at STA. This occurs in both pristine SIRs and hybrid events. In a small number of SIRs, the shock occurs within the SIR rather than near the edges, for example, the 18 – 22 May 2012 SIR at STB, the 29 – 31 March 2014 SIR at STB, and the 18 – 20 August 2016 SIR at STA.

3. Comparison of SIRs with and Without an HCS Crossing

The slow and dense solar wind between fast-wind streams has long been believed to be the interplanetary counterparts of coronal streamers that are clearly visible on the limb of the

Table 1 Comparison of SIR properties between the SIRs with and without HCS.

Parameter	Mean		Median	
	SIRs with HCS	SIRs without HCS	SIRs with HCS	SIRs without HCS
Number of SIRs	278	176	–	–
Shock rate [%]	30	27	–	–
N_{pmax} [cm^{-3}]	$29.8 \pm 0.9^{*}$	23.0 ± 1.1	26.9	20.0
V_{min} [$km\,s^{-1}$]	320 ± 2	335 ± 3	310	327
V_{max} [$km\,s^{-1}$]	568 ± 6	587 ± 7	568	600
B_{max} [nT]	13.2 ± 0.2	12.4 ± 0.3	12.5	12.0
P_{tmax} [pPa]	153 ± 5	136 ± 6	132	120
P_{dynmax} [nPa]	8.2 ± 0.3	6.9 ± 0.3	7.3	6.1

*The uncertainty is the standard error of the mean

Sun (*e.g.* Feldman *et al.*, 1981; Gosling *et al.*, 1981; Bavassano, Woo, and Bruno, 1997). There are two types of coronal streamers: helmet or dipolar streamers, which separate coronal holes of opposite magnetic polarity, and pseudo-streamers, which separate holes of the same polarity (Wang, Sheeley, and Rich, 2007). The cusp of a helmet streamer coincides with the inner edge of an HCS.

To investigate the effect of different origins of slow wind on the SIRs, we have examined the distribution of magnetic-field sectors around each SIR using magnetic-field data and pitch-angle distribution of suprathermal electrons, and sorted SIRs into two groups: with an HCS crossing within three days of stream interface, and without an HCS crossing. We have also checked the synoptic field and coronal-hole maps from the *Global Oscillation Network Group* (GONG: gong.nso.edu/) of the National Solar Observatory (Harvey *et al.*, 1996; Leibacher, 1999) and from Predictive Science Inc. (www.predsci.com/stereo/) to track down the probable source regions. Although there is some discrepancy among results using different coronal models and different photospheric magnetograms (*e.g.* Jian *et al.*, 2011, 2015, 2016), the connection of the *in-situ* observations to the aforementioned synoptic maps generally supports the assumption that the SIRs with and without HCS originate from the regions related to the helmet streamers and pseudo-streamers, respectively (Crooker *et al.*, 2012).

The pitch-angle distribution of suprathermal electrons and magnetic-field direction are variable around the HCS, so there are occasional short magnetic-field sectors, lasting fewer than three days. This is observed in the slow-wind side of 47 SIRs, in the fast-wind side of seven SIRs, and in both sides of three SIRs. In the other seven SIRs, the whole SIR is embedded within a short magnetic sector or vice versa. In one SIR, the association with HCS cannot be determined due to a data gap. Excluding the cases with magnetic sectors shorter than three days, among the 518 pristine SIRs with available data, 278 (54%) SIRs are associated with a clear HCS crossing; and 176 (34%) SIRs are not associated with any HCS crossing.

Among the 278 pristine SIRs with clear HCS crossings, 30% of them drive shocks. The shock-association rate is slightly higher than 27% for the 176 pristine SIRs without clear HCS crossings. Figure 4 displays the comparison of the histograms of six SIR properties between the cases with (blue bars) and without HCS crossing (orange bars). Table 1 lists the comparison of the mean and median values of these parameters between the two groups of SIRs. In contrast to the SIRs without an HCS crossing, the SIRs with an HCS crossing generally have higher maximum proton number density [N_{pmax}] and slightly higher peak

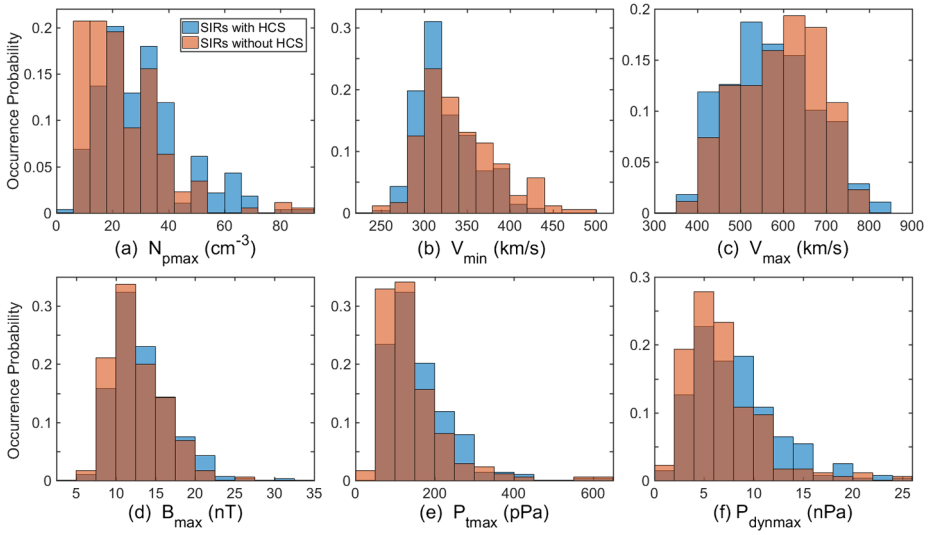

Figure 4 The comparison of occurrence probabilities between SIRs with an HCS crossing (*blue bars*) and without any HCS crossing (*orange bars*) for the following parameters: (**a**) maximum N_p, (**b**) minimum speed, (**c**) maximum speed, (**d**) maximum B, (**e**) peak P_t, and (**f**) peak dynamic pressure. The *brown shaded* regions are the overlapping regions between SIRs with an HCS and the SIRs without any HCS crossing.

magnetic field [B_{max}], resulting in stronger compression of P_t. These results are consistent with the conclusions of Borovsky and Denton (2013) based on a superposed epoch analysis of 74 helmet streamer CIRs *versus* 11 pseudo-streamer CIRs, all of which drove geomagnetic storms. They are also in agreement with the cumulative-distribution comparison between 84 dipolar streamers and 44 pseudo-streamers of Crooker, McPherron, and Owens (2014).

Two factors could contribute to a higher N_{pmax} in SIRs with an HCS than SIRs without an HCS. First, the HPS around the HCS are usually dense. Second, the helmet streamers are observed to emit blobs of dense plasma near the Sun (Wang *et al.*, 2000; Foullon *et al.*, 2011) while pseudo-streamers are not (Wang *et al.*, 2012). Wang *et al.* (2012) argued this was because the convergence of like-polarity field lines above the X-point of pseudo-streamers would prevent the underlying loops from expanding outward and pinching off. However, blob-like structures are found to be embedded within SIRs without HCS, such as the one in Figure 15a. Owens, Crooker, and Lockwood (2013) found the occurrence rates of large-scale inverted heliospheric magnetic field were similar at dipolar streamers and pseudo-streamers and suggested that the rate of reconnection was set externally, possibly by the differential-rotation rate that governed the circulation of open solar flux.

As displayed in Figure 4 and Table 1, the minimum and maximum speeds are both slightly slower in SIRs with an HCS than in SIRs without an HCS. The peak dynamic pressure [P_{dynmax}] is higher in SIRs with an HCS than SIRs without an HCS, mostly due to higher density. The duration, speed increase, and average acceleration rate crossing an SIR are statistically similar between the SIRs with and without an HCS, which are not illustrated or tabulated here. On the other hand, it is reported that the fast wind typically lasts longer beyond the compression region for SIRs with an HCS than for SIRs without an HCS (Neugebauer *et al.*, 2004; Borovsky and Denton, 2013), which is attributed to larger coronal

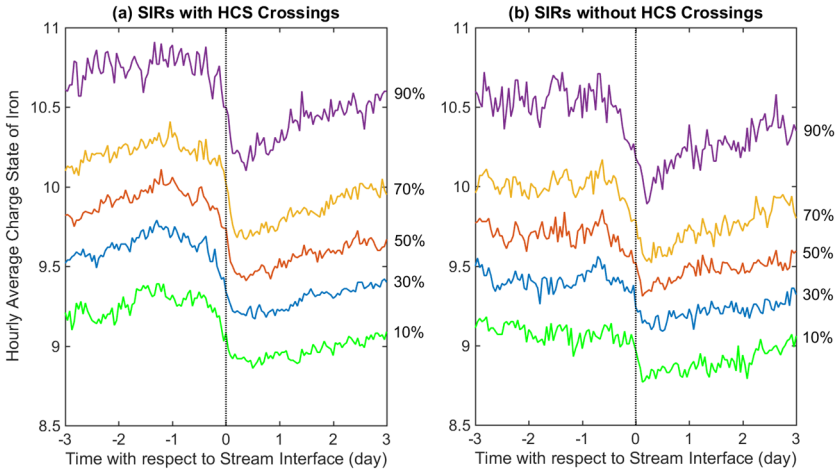

Figure 5 The distribution of hourly average charge state of iron within ± three days of the stream interface (*black-dotted vertical line*) for pristine SIRs observed at STA in 2007 – 2016 through superposed epoch analysis: (**a**) 186 SIRs with HCS crossings, (**b**) 103 SIRs without HCS crossings. The percentile ranks are marked by the *color solid lines* (*red* for the median values), and the percentages are given on the *right* side. For example, the 10% line indicates that 10% of SIRs have $\langle Q_{\mathrm{Fe}} \rangle$ lower than the value along the *green line* at each hourly time step.

holes associated with helmet streamers and also to the spacing of the same-polarity source regions being closer than that of the source regions separated by an HCS.

Heavy-ion charge states measured *in situ* are indicative of the hot-electron temperature in the coronal sources. For example, the O^{7+}/O^{6+} ratio is typically higher in the solar wind originating from helmet streamers than the wind from the coronal holes, and the O^{7+}/O^{6+} ratio falls between the two extremes for solar wind from other sources, such as active regions and quiet Sun (*e.g.* Zhao *et al.*, 2017). So far, the validated heavy-ion data from STEREO are only for iron (Galvin *et al.*, 2009), and STA provides hourly data on iron charge state [Q_{Fe}] throughout the mission, while two-hour data are available for STB up to July 2011. Next we analyze the 291 pristine SIRs only from STA observations with available suprathermal-electron data needed for HCS identification.

Figure 5 compares the distributions of hourly average charge states of iron [$\langle Q_{\mathrm{Fe}} \rangle$] within ± three days of the stream interface for SIRs with and without an HCS crossing, excluding the cases of short magnetic sectors. In the superposed epoch analysis, the time series of $\langle Q_{\mathrm{Fe}} \rangle$ from different SIRs are organized in an ensemble with epoch zero corresponding to the SI. At each hourly time step from negative three to positive three days, the statistics from the ensemble are obtained including the values at different percentile ranks. For example, the 10% line indicates 10% of the SIRs have $\langle Q_{\mathrm{Fe}} \rangle$ lower than the values along the green line at each time step, and the 90% line indicates 90% of the SIRs have $\langle Q_{\mathrm{Fe}} \rangle$ lower than the values along the purple line at each time step. The 50% line marks the median value at each time step from three days before to three days after the stream interface.

As shown in Figure 5, the $\langle Q_{\mathrm{Fe}} \rangle$ decreases relatively sharply at the SI, typically by about half a unit across four to five hours. Regardless of HCS association, the $\langle Q_{\mathrm{Fe}} \rangle$ is higher in the slow wind before SI than in the fast wind after the SI. In comparison with the SIRs associated with HCS crossings, the $\langle Q_{\mathrm{Fe}} \rangle$ is lower throughout the SIRs without HCS crossings, by about 1/3 of a charge unit at most. The $\langle Q_{\mathrm{Fe}} \rangle$ hump within two days ahead of SI is prominent in the SIRs with an HCS, probably attributed to the origin related to the helmet streamers.

In the source regions surrounding pseudo-streamers, the iron charge state hardly changes on the slow-wind side. Crooker, McPherron, and Owens (2014) found similar differences using the ionic composition ratios of O^{7+}/O^{6+} and C^{6+}/C^{5+} and the elemental composition ratio of Fe/O.

4. Solar-Cycle Variations of SIR Properties

SIRs are one major type of solar-wind structure in addition to ICMEs affecting the Earth and other planets, and cumulatively they occur more often than ICMEs. It is important to investigate their solar-cycle dependence, especially for this weakest cycle in the Space Age when SIRs represent some of the strongest solar-wind parameter enhancements. In combination with our previous survey of SIRs at the Lagrange point 1 (L_1) in 1995 – 2009 using *Wind* and ACE data based on the same criteria (Jian *et al.*, 2006a; Jian, Russell, and Luhmann, 2011), we study the variations of SIR properties with solar activity from 1995 to 2016. In Figures 6 – 8, the top panels show the recently corrected monthly sunspot number (SSN) from the Sunspot Index and Long-term Solar Observations (SILSO: www.sidc.be/silso/). The maximum SSN in this cycle is about 2/3 of the last SSN maximum. In Cycle 24, the two SSN peaks are separated by more than two years, due to the different evolution paces in the two hemispheres (*e.g.* Temmer *et al.*, 2006 and the references therein), as shown in the plot of hemispheric sunspot numbers at www.sidc.be/silso/monthlyhemisphericplot. The cyan horizontal bars at the top of Figures 6 – 8 mark the comparable phases in these two cycles covering from the solar minimum to the middle of the declining phase: July 1996 – June 2004 for Cycle 23; January 2009 – December 2016 for Cycle 24. The blue-vertical bars indicate the L_1 SIR survey, and the red vertical bars denote the STEREO survey.

In the second panel of Figure 6, the filled bars indicate the number of CIRs, and the whole bars including filled and empty areas mark the count of SIRs. We observe slightly more SIRs in this cycle than in the previous cycle. The STA data are fully available only for 1.5 months in 2015 because of the data gap and reduced coverage associated with solar conjunction. We normalize the occurrence rate for 2015, admitting that there is a large uncertainty. The STA data are fully available in 2016, and 57 SIRs are observed, more than any other year since 1995. Meanwhile, the ICME count in 2016 is surprisingly low in contrast with the similar phase of the previous cycle (Jian *et al.*, 2018). We will keep tracking the SIR and ICME occurrence for the rest of this solar cycle when more data become available. In both cycles, fewer SIRs are observed around solar maximum, and the solar-cycle dependence may be somewhat stronger if we apply thresholds of maximum speed [V_{max}] and speed increase in the SIR selection, as illustrated in Figure 9 of Jian, Russell, and Luhmann (2011).

The CIR rate (the same as the SIR recurrence rate) is noticeably higher in this cycle than the previous one, probably because of persistent equatorial coronal holes as well as fewer and weaker ICMEs in this cycle (*e.g.* Chi *et al.*, 2016; Jian *et al.*, 2018). Using the OMNI magnetic-field data (King and Papitashvili, 2005), L. Svalgaard has identified slightly fewer HCS crossings in this cycle than in the last cycle (wso.stanford.edu/SB/SB.Svalgaard.html), with the average annual HCS count declining from 28 to 26.5. In response, there are slightly fewer SIRs associated with the HCS in Cycle 24 than in Cycle 23. The HCS association rate of SIRs from 2009 – 2016 is on average 49%, lower than the rate of 57% in the comparable phase of the last cycle, marked by the cyan-dashed line in the last panel of Figure 6. Note that we require magnetic sectors at the two sides of an HCS lasting longer than three days. In 2009 – 2016, about 35% of SIRs are clearly not associated with any HCS, while about 12% of SIRs have magnetic sectors shorter than three days, most often in the slow-wind

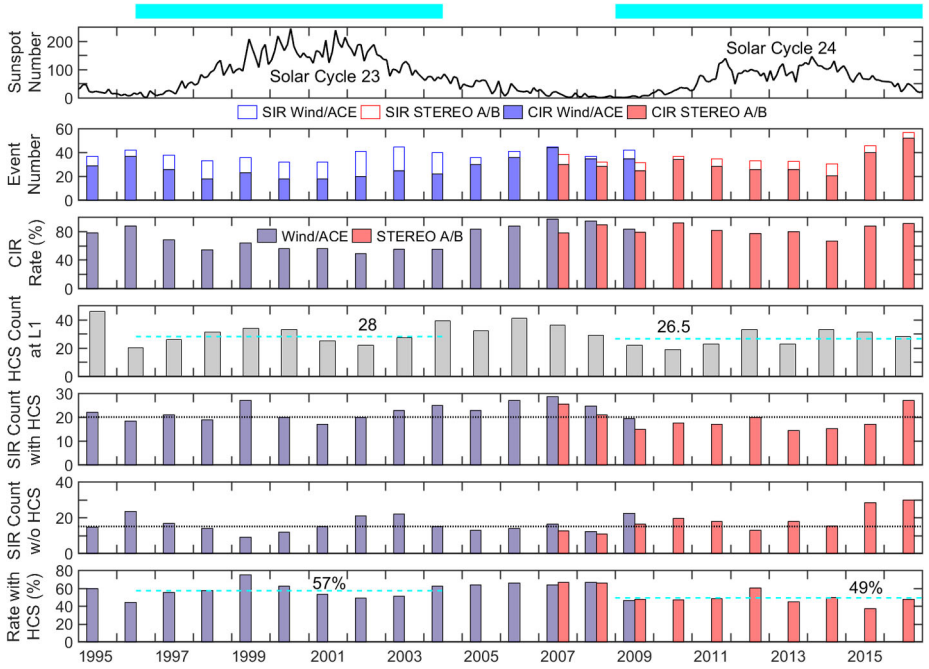

Figure 6 Variations of the annual averages of SIR properties from 1995 to 2016. From *top* to *bottom*: monthly sunspot number, SIR (*whole bar*) and CIR (*filled bar*) number, CIR rate, HCS count from the list compiled using the OMNI magnetic-field data, count of SIRs with an HCS (*black-dotted line* marking 20), count of SIRs without any HCS crossing (*black-dotted line* marking 15), HCS association rate for SIRs. The *cyan horizontal bars* at the *top* mark the comparable phases of Solar Cycles 23 and 24. The *blue bars* indicate the results from *Wind*/ACE survey in 1995 – 2009, and the *red bars* denote the results from STEREO-A/B survey in 2007 – 2016. The *cyan-dashed horizontal lines* in the fourth and last *panels* mark the averages for these two phases with the average values indicated.

side. The higher rate of non-HCS association indicates more pseudo-streamers in this cycle than in the comparable phase of the last cycle.

Table 2 compares the mean and median values of six SIR parameters between the similar phases of Cycles 23 and 24. The mean values are also marked by cyan-dashed horizontal lines in Figures 7 and 8. The minimum speed [$V_{\rm min}$], $V_{\rm max}$, $B_{\rm max}$, $P_{\rm tmax}$, and $P_{\rm dynmax}$ are all lower in this cycle than in the last cycle. The decline of $V_{\rm max}$ may be partly due to weaker polar coronal holes and fewer SIRs associated with them. The decrease fractions of these parameters are slightly less than the decrease fractions of the general solar wind using daily OMNI data for Cycle 23 and daily STEREO data for Cycle 24, except for the similar declining fractions for $V_{\rm min}$ within SIRs and background solar-wind speed. This suggests that SIRs weaken less than the background solar wind, similar to the findings for ICMEs of Jian *et al.* (2018). Despite the decreases of $V_{\rm min}$ and $V_{\rm max}$, the speed enhancements [$\Delta V = V_{\rm max} - V_{\rm min}$] across SIRs are similar between the two comparable phases of Cycles 23 and 24.

Due to a slower $V_{\rm min}$ and $V_{\rm max}$, the mean speed of SIRs (estimated using the average of $V_{\rm min}$ and $V_{\rm max}$) is also slower in this cycle than in the previous one. Following Figure 1 of Jian *et al.* (2008a), we compute the product of the mean speed, duration, and the sine of the spiral angle, and use it to estimate the projected width perpendicular to the stream interface in the solar equatorial plane. Despite a slight decrease of mean speed, the SIRs

Table 2 Comparison of SIR properties in similar phases of Solar Cycles 23 and 24: from the solar minimum to the middle of declining phase.

Category	Parameter	Using average values			Using median values		
		Cycle 23	Cycle 24	Decrease fraction [%]	Cycle 23	Cycle 24	Decrease fraction [%]
SIR using STEREO for Cycle 24	B_{max} [nT]	15.5 ± 0.3	13.3 ± 0.2	15 ± 2	14.5	12.5	14
	P_{tmax} [pPa]	175 ± 6	147 ± 4	16 ± 4	140	125	11
	V_{min} [km s^{-1}]	357 ± 3	323 ± 2	9 ± 1	350	320	9
	V_{max} [km s^{-1}]	587 ± 6	556 ± 5	5 ± 1	580	553	5
	ΔV [km s^{-1}]	230 ± 5	233 ± 4	-1 ± 3	220	227	−3
	P_{dynmax} [nPa]	8.8 ± 0.3	7.3 ± 0.2	16 ± 4	7	6	14
General solar wind using STEREO for Cycle 24	B [nT]	6.8 ± 0.1	5.26 ± 0.03	23 ± 1	6.2	4.7	24
	P_t [pPa]	22.3 ± 0.3	15.4 ± 0.2	31 ± 1	18.7	12.3	34
	V [km s^{-1}]	442 ± 2	401 ± 1	9.4 ± 0.5	423	382	10
	P_{dyn} [nPa]	2.27 ± 0.03	1.52 ± 0.02	33 ± 1	1.98	1.19	40
General solar wind using OMNI for both Cycles	B [nT]	6.8 ± 0.1	5.44 ± 0.04	20 ± 1	6.2	5	19
	P_t [pPa]	22.3 ± 0.3	19.2 ± 0.2	14 ± 1	18.7	15.8	16
	V [km s^{-1}]	442 ± 2	410 ± 2	7 ± 1	423	392	7
	P_{dyn} [nPa]	2.27 ± 0.03	1.82 ± 0.02	20 ± 1	1.98	1.54	22

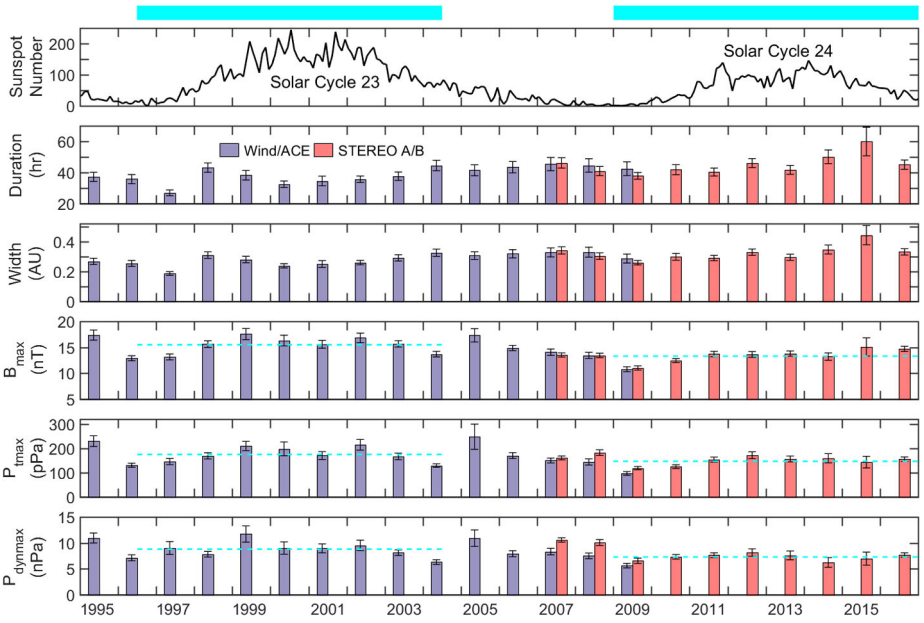

Figure 7 Variations of the annual averages of SIR properties from 1995 to 2016. From *top* to *bottom*: monthly sunspot number, duration, width, maximum magnetic-field intensity, maximum total pressure, maximum dynamic pressure. The *cyan horizontal bars* at the *top* mark the comparable phases of Solar Cycles 23 and 24. The *blue bars* indicate the results from *Wind*/ACE survey in 1995 – 2009, and the *red bars* denote the results from STEREO-A/B survey in 2007 – 2016. The *error bar* indicates the standard error of the mean. The *cyan-dashed lines* in the last three *panels* mark the averages for the comparable phases of the two cycles, which are listed in Table 2.

are moderately wider in Cycle 24 than in Cycle 23, mainly because of longer duration in this cycle. The wider span of SIRs is possibly in part due to the background solar wind weakening more than the SIRs in this cycle.

Using 27-day average OMNI data, we calculate the magnetosonic speed [V_{ms}] of the solar wind at L_1, and use it as an approximation for the near 1-AU solar wind. As shown in the fifth panel of Figure 8, the V_{ms} is generally slower in the comparable phase of Cycle 24 than in Cycle 23. Although the peak total pressure and dynamic pressure are weaker for SIRs in this cycle, their shock rate (32%) turns out to be higher than the rate of 25% for the last cycle, possibly due to slower V_{ms} in the background solar wind. In addition, the shock-association rate of SIRs seems to have followed the SSN better thus far in this cycle than in the last cycle.

Figure 3 illustrates the solar-cycle variations of the associated shock rates for all SIRs and pristine SIRs from 2007 to 2016. The total shock rate roughly follows the sunspot activity, being higher around solar maximum, mostly because of forward shocks. If we only consider the pristine SIRs to exclude the complication of ICME interaction and questionable events, the forward-shock rate still shows moderate solar-cycle dependence. Only eight SIRs are observed in 2015 because of the long data gap around solar conjunction, and two SIRs drove shocks; thus the results in 2015 carry large uncertainty. The rate of only reverse shocks (green bars) does not vary much over the ten years except in 2012 and 2014. In some years, the forward- and reverse-shock occurrence rates are comparable, for example, in 2009 – 2011 (the rising phase of Cycle 24), when the count for either forward or reverse shocks

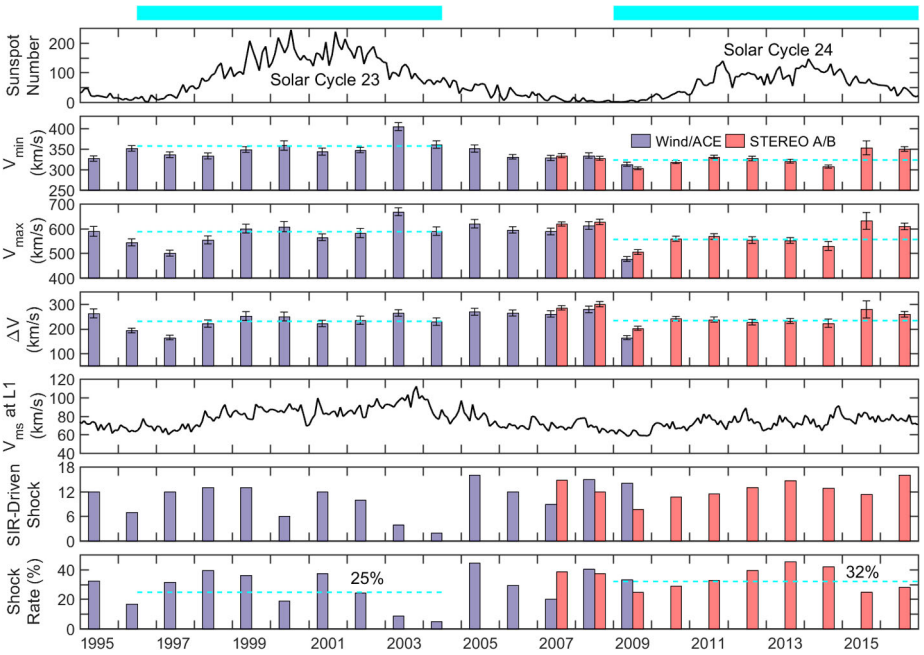

Figure 8 Variations of the annual averages of SIR properties from 1995 to 2016. From *top* to *bottom*: monthly sunspot number, minimum speed, maximum speed, speed increase across SIR, magnetosonic speed in the solar wind from OMNI data, count of SIRs associated with shocks, shock rate of SIRs. The *cyan horizontal bars* at the *top* mark the comparable phases of Solar Cycles 23 and 24. The *blue bars* indicate the results from *Wind*/ACE survey in 1995 – 2009, and the *red bars* denote the results from STEREO-A/B survey in 2007 – 2016. The *error bar* indicates the standard error of the mean. The *cyan-dashed horizontal lines* mark the averages for the comparable phases of the two cycles, which are listed in Table 2.

was at least seven per year. The equal role or predominance of reverse shocks in some years (2005 – 2006) was not emphasized in our previous L_1 survey (Jian, 2008), partly due to low statistics, *e.g.* only three or four reverse shocks per year. Now, with the twin STEREO spacecraft, we have obtained better statistics and revealed that forward shocks do not always prevail over reverse shocks at SIRs.

5. Dual Observations of SIRs in 2007 – 2014

5.1. STA–STB Orbital Difference and the Dual-Observed SIR Database

In their journeys orbiting the Sun, the latitudinal difference between the twin STEREO spacecraft varies within $\pm 15°$ as shown in Figure 9a, due to the inclination of the Heliographic Equator with respect to the Ecliptic. The twin spacecraft crossed their paths at the far side of the Sun on 21 March 2015. The orbit from 1 January 2007 to 21 March 2015 is indicated by the blue curved line, and the green line represents the orbit from 22 March 2015 to the end of 2017. The latitudinal difference between the twin spacecraft [$\Delta\theta$] increases with the increase of their smaller longitudinal separation [$\Delta\varphi$] in the range of 0° – 180°, reaching its maximum value around February 2011 when the twin spacecraft are 180° apart in longitude. As illustrated in Figure 9b, the difference of their radial distances varies around

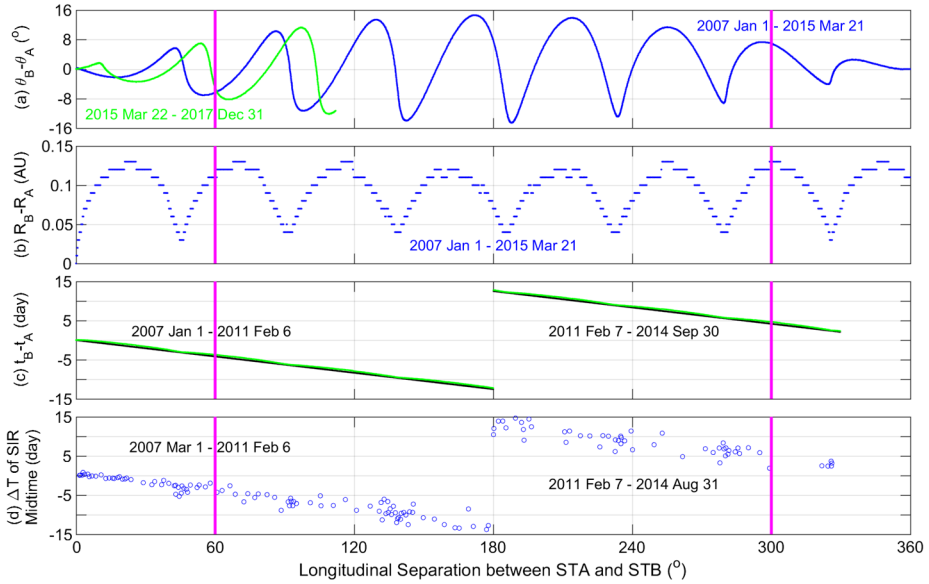

Figure 9 The orbital difference and solar-wind arrival time offset between STEREO-A and -B spacecraft as a function of their longitudinal separation: (**a**) latitudinal difference, (**b**) difference of heliocentric distance, (**c**) expected time difference, (**d**) the time difference of SIR middle time. The orbital data are in the HGI coordinate. In (**c**), the *black line* indicates the expected time difference from the longitudinal separation, and the *green line* marks the expected time from Equation 1 including additional propagation time due to radial difference. In (**d**), each *circle* denotes one SIR pair observed by both STA and STB. The positive ΔT indicates SIRs occurring later at STB than STA. The *magenta-solid vertical lines* in each *panel* mark the acute longitudinal separation of 60°, the same separation as an L_4 or L_5 mission with respect to the Earth.

0.02 – 0.14 AU, with STB always at a greater heliocentric distance than STA. The black line in Figure 9c indicates the expected time delay [Δt] for the same solar-wind flow rotating from STB to STA (when $\Delta\varphi$ is not more than 180°) or from STA to STB (when $\Delta\varphi$ is greater than 180°) before contact with STB was lost. The green line in the same panel marks the expected time delay including additional propagation time from STA to STB assuming solar-wind speed of 450 km s^{-1}. For the largest radial difference of 0.14 AU, the propagation time from STA to STB would be 0.54 day, shorter than the rotational time offset when $\Delta\varphi$ exceeds about 7.8°.

Full plasma-data coverage of STA paused near the end of August 2014 and resumed in November 2015. In the period of March 2007 – August 2014, we match the dual observations for the same pristine SIRs, considering the time shift in Equation 1 and taking the mean speed of each SIR at STA as the solar-wind speed. Because the stream interface is not always near the center of an SIR, we compare the middle times of SIRs. Allowing the expected and observed time to differ by one to four days, we find 96, 129, 151, and 161 SIR pairs, respectively. To be relatively inclusive, we select a temporal window of three days, and we verify that the results are mostly consistent with the manual comparison. For a mission located at Lagrange point 4 (L_4) or 5 (L_5), the longitudinal separation from the Earth would be 60°, and the time offset would be about two to five days depending on the exact orbit and solar-wind speed, as marked by the circles near the magenta vertical lines in Figure 9d.

As shown in Figure 10, the annual SIR counts are not always the same between STA and STB from 2007 to 2014, differing by up to ten in 2011 and 2014 near solar maximum.

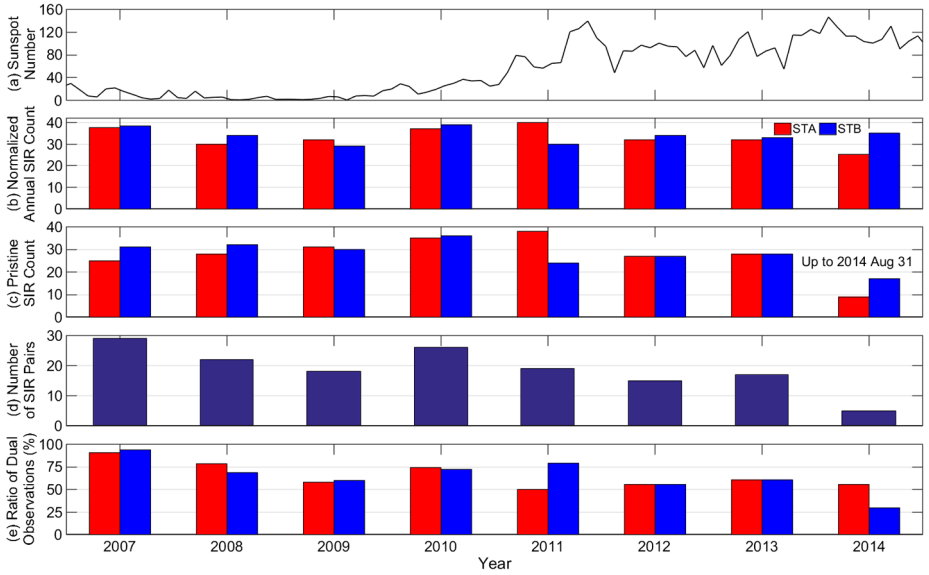

Figure 10 Variation of (**a**) monthly sunspot number, (**b**) normalized annual SIR count, (**c**) pristine SIR count (not normalized to one year, up to 31 August 2014), (**d**) number of SIR pairs, and (**e**) the ratio of dual-observed SIRs among the total pristine SIRs. The *red and blue bars* indicate STA and STB, respectively.

This could be partly due to the interruption by CMEs and other transient events. As the solar activity rises, the annual count of SIR pairs decreases from 2007 to 2014, except in 2010. The fraction of dual-observed SIRs among pristine SIRs varies from 30 % to 90%, generally higher when the twin spacecraft are closer and the Sun is less active, such as 2007 – 2008. The fractions differ substantially between STA and STB in 2011 and 2014, associated with the large discrepancy of pristine SIR counts between the twin spacecraft in these two years. In 2014, STA observed nine fewer pristine SIRs than STB, partly because contemporaneously 13 more ICMEs were encountered at STA than STB.

The scatter plots in Figure 11 display the comparison of the SIR parameter values at STA and STB. There are a total of 151 SIR pairs. Because of orbital differences (radial, latitudinal, and longitudinal), temporal changes of solar-wind sources (*e.g.* Simunac *et al.*, 2009; Heinemann *et al.*, 2018), and evolution in the interplanetary medium, the parameters at the two spacecraft can be very different at times. Among the six parameters listed in Figure 11, the $V_{\max}$ is best correlated between the dual observations, with a Pearson correlation coefficient of 0.57. In contrast, Opitz *et al.* (2009) found the correlation of solar-wind speed is 0.95 for a time lag of 0.5 days and 0.85 for two days in the early phase of the STEREO mission (2007 March – August). The N_{pmax} is the least correlated, with a correlation coefficient of 0.12. The correlation does not improve much if we reduce the time-offset window to one to two days.

5.2. Comparison Between the Dual Observations

We plot the differences of parameter values at STB and STA *versus* the radial difference between the two spacecraft in Figure 12. The parameter values are generally evenly spread around zero, except that there are more circles below the zero line for the maximum proton number density and dynamic pressure. Table 3 lists the quantitative comparison between

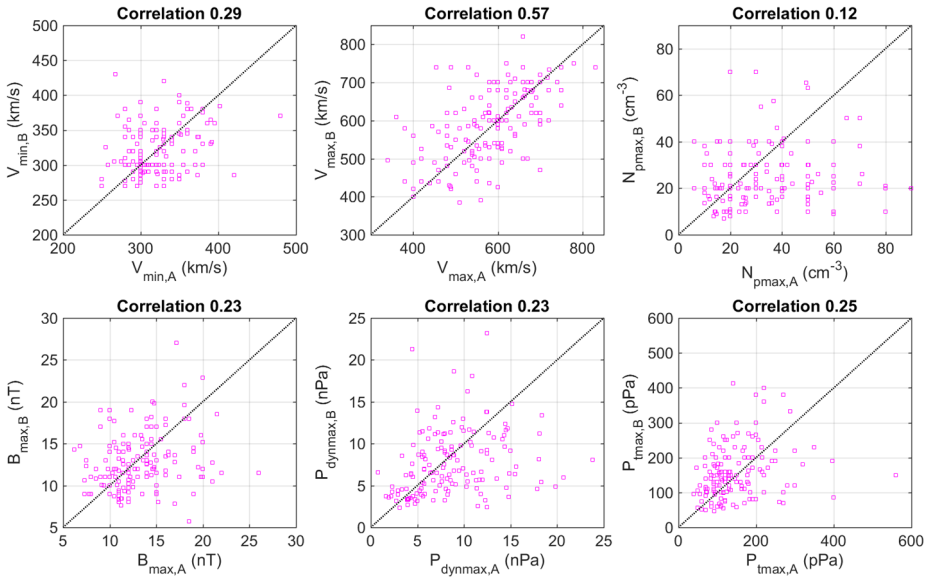

Figure 11 The scatter plots of six SIR parameters: $V_{\rm min}$, $V_{\rm max}$, $N_{\rm pmax}$, $B_{\rm max}$, $P_{\rm dynmax}$, and $P_{\rm tmax}$. The *abscissa* is the parameter at STA, and the *vertical axis* is the parameter at STB. Each *square* marks one SIR pair. In each *panel*, *the black-dotted line* indicates the best correlation. The correlation coefficients are listed at the *top* of each *panel*.

Table 3 Statistics of 151 SIR pairs observed by both STA and STB in March 2007 – August 2014.

Parameter	Mean		Median	
	STA	STB	STA	STB
Shock rate [%]	30	28	–	–
$N_{\rm pmax}$ [cm^{-3}]	33 ± 1	25 ± 1	30	21
$V_{\rm min}$ [km s^{-1}]	322 ± 3	321 ± 3	315	310
$V_{\rm max}$ [km s^{-1}]	579 ± 8	588 ± 8	580	590
$B_{\rm max}$ [nT]	13.3 ± 0.3	12.8 ± 0.3	12.5	12.1
$P_{\rm tmax}$ [pPa]	146 ± 6	157 ± 6	120	144
$P_{\rm dynmax}$ [nPa]	8.7 ± 0.4	7.8 ± 0.3	8.1	6.8

STA and STB observations for the 151 SIR pairs. The $N_{\rm pmax}$ is lower at STB than STA, on average by $24 \pm 4\%$, as expected by its greater heliocentric distance. The associated $P_{\rm dynmax}$ is slightly lower at STB than at STA, by about 10%. Although the median of $P_{\rm tmax}$ is higher at STB than at STA, its mean is very similar to STA, considering the standard error of the mean. SIR shocks develop with heliocentric distance, rising from a shock rate of 3% at 0.72 AU (Jian *et al.*, 2008a, 2008b) to 91% at 5.3 AU (Jian *et al.*, 2008c). Although STB is slightly farther away from the Sun than STA, the small radial difference of 0.02 – 0.14 AU does not systematically affect the shock rate. Their shock rates are quite similar, at around 30%. With a mixture of SIRs from STA and STB, the small differences caused by the radial difference should not affect the comparison results in Section 4 using *Wind*/ACE data for Cycle 23 and STEREO observations for Cycle 24.

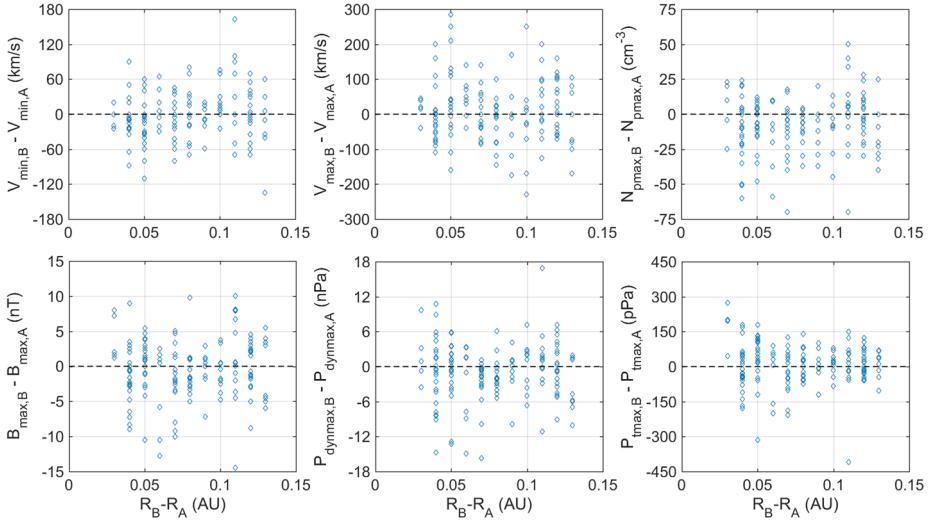

Figure 12 The scatter plots of six SIR parameters: $V_{\rm min}$, $V_{\rm max}$, $N_{\rm pmax}$, $B_{\rm max}$, $P_{\rm dynmax}$, and $P_{\rm tmax}$. The *abscissa* is the difference of heliocentric distance from STA to STB, and the *vertical axis* is the difference of parameter values between STA and STB. In each *panel*, the *black-dashed horizontal line* marks zero.

Next we compare the differences of parameter values at STB and STA *versus* their latitudinal difference, as shown in Figure 13. The SIRs observed when the twin spacecraft are in the same hemisphere according to the HGI coordinates are marked by red circles, while the SIRs observed when the twin spacecraft are in different hemispheres are marked by blue circles. For 44% of the time, the latitudinal offset between the twin STEREO spacecraft is less than 5° (bounded by the pair of vertical dashed lines in Figure 13), and the parameter distributions are slightly less scattered with somewhat smaller standard deviations than during larger latitudinal offset. This is expected because the solar wind is more likely to originate from different parts of the Sun when the latitudinal offset is large. Several cases of large parameter discrepancy are marked by filled circles with their dates at STA noted, to facilitate the verification and investigation of these events.

Figure 14 illustrates dual observations of an SIR pair as one example when the maximum proton number density and dynamic pressure have large discrepancies between STA and STB observations, although the two spacecraft are separated by only 4.8° in latitude. The HCS occurred within the SIR on 24 – 25 April 2008 at STA, but it occurred one day before the start of the SIR at STB. Probably partly due to the HPS surrounding the HCS, similar to the case in Figure 1, the compression of proton number density, dynamic pressure, magnetic field, and total pressure is much stronger at STA than at STB.

On the other hand, the compression of SIRs may also depend on the attack angle of the fast-wind flow with the slow wind ahead. Assuming there is no interpenetration of solar-wind streams, strong shear flow takes place at the conventionally defined stream interface, as shown in Figure 11 of Gosling and Pizzo (1999). Because the radial component of solar-wind velocity is generally much faster than the other components, this attack angle can be approximated by the tilt of the velocity-deflection structure relative to the radial direction. A higher tilt to the radial direction would imply a stronger attack if other solar-wind properties such as the speed and density are the same.

At STA, there is evident flow deflection at the sharp discontinuity indicated by the cyan dash–dotted line. Conducting minimum variance analysis (MVA) (Sonnerup and Cahill,

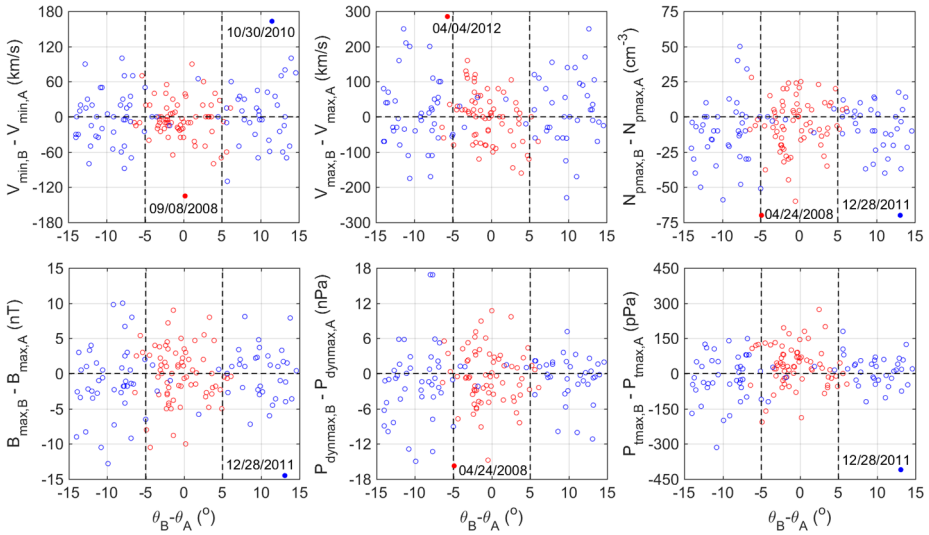

Figure 13 The scatter plots of six SIR parameters: $V_{\rm min}$, $V_{\rm max}$, $N_{\rm pmax}$, $B_{\rm max}$, $P_{\rm dynmax}$, and $P_{\rm tmax}$. The *abscissa* is the latitudinal difference from STA to STB, and the *vertical axis* is the difference of parameter values between STA and STB. The *red circles* mark the SIRs when the twin spacecraft are in the same hemisphere, and the *blue circles* indicate the SIRs when the twin spacecraft are in different hemispheres. In each *panel*, the *black-dashed horizontal line* marks zero, and the *black-dashed vertical lines* mark the latitudinal difference of $\pm 5°$. The extreme cases are denoted by the *filled circles* with the dates at STA marked.

1967) across 15:58 – 16:16 UT on 24 April using solar-wind velocity vector data, we determine the normal direction of the velocity-deflection structure is $0.709\hat{\boldsymbol{R}}+0.705\hat{\boldsymbol{T}}-0.019\hat{\boldsymbol{N}}$, where $\hat{\boldsymbol{R}}$, $\hat{\boldsymbol{T}}$, and $\hat{\boldsymbol{N}}$ are unit vectors in the radial–tangential–normal (RTN) coordinates (Fränz and Harper, 2002). The velocity deflection is less evident at STB. Conducting the MVA across 11:53 – 12:53 UT (longer duration is selected because of embedded data gap and in order to meet the criterion that the eigenvalue ratios should be greater than two) on 22 April using velocity vector data, we find the normal direction of the velocity-deflection plane is $0.982\hat{\boldsymbol{R}}+0.014\hat{\boldsymbol{T}}+0.189\hat{\boldsymbol{N}}$, more aligned with the radial direction than the normal direction at STA, suggesting the stream interface is more perpendicular to the solar-wind flow at STB than STA. At STA and STB, the slow-wind streams in the two- to three-hour temporal window upstream of the interface are in the directions of $0.999\hat{\boldsymbol{R}}+0.012\hat{\boldsymbol{T}}+0.023\hat{\boldsymbol{N}}$ and $0.988\hat{\boldsymbol{R}}+0.141\hat{\boldsymbol{T}}-0.048\hat{\boldsymbol{N}}$, respectively, confirming the assumption of radial flow direction. Although the stream interface is less tilted relative to the solar-wind flow at STA, much faster solar wind may have caused greater compression there. A forward shock is formed at the leading edge of the SIR at STA. Field inversions (transient flips of field polarity) mentioned above in Section 2 appear frequently not only near HCS, but also throughout the SIR and in the trailing fast wind.

Another SIR pair with a large discrepancy between dual observations occurred on 28 December 2011 at STA and on 6 – 8 January 2012 at STB, as displayed in Figure 15. STB was 0.11 AU farther away from the Sun than STA, and the twin spacecraft were 14.1° apart in latitude and 151° apart in longitude. This is close to the situation when the twin spacecraft are farthest separated. The SIR lasts more than one day longer at STB than at STA, while the $N_{\rm pmax}$, $P_{\rm dynmax}$, and $P_{\rm tmax}$ at STB are only about one quarter of the values at STA. There is no HCS crossing nearby at STA. According to the pitch-angle distribution of suprathermal

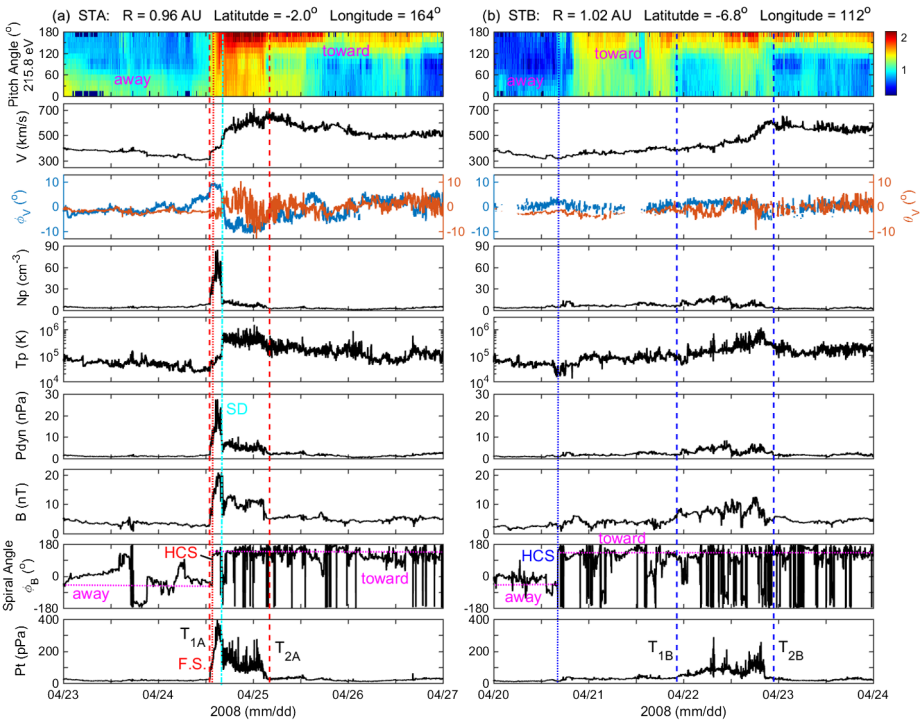

Figure 14 One example of dual observations of SIRs at (**a**) STA and (**b**) STB. The captions of Figure 1 apply, except the sixth panel is dynamic pressure, not entropy. Note that suprathermal-electron flux at 215.8 eV is used in the first *panel*. In (**a**), the pair of *red-dashed vertical lines* mark the boundaries of the SIR at STA (T_{1A} and T_{2A}); the *red-dotted vertical line* indicates the HCS; and the *cyan dash–dotted vertical line* denotes the sharp discontinuity (SD) between slow- and fast-wind streams. In (**b**), the pair of *blue-dashed vertical lines* marks the boundaries of SIR at STB (T_{1B} and T_{2B}), and the *blue-dotted vertical line* indicates the HCS. In (**a**) and (**b**), the toward and away sectors are marked by the *magenta-dotted horizontal lines* in the spiral-angle *panel*.

electrons in the top panel of Figure 15b, a 1.5-day magnetic sector of away polarity appears in the slow-wind part of the SIR at STB, while the magnetic field is in the toward sector for over three days at either side of this short sector. The directional changes of Parker-spiral angle are more variable and not shown in Figure 15. Although the fast wind only reaches about 500 km s^{-1} and 450 km s^{-1} at STA and STB, respectively, the proton number density and temperature demonstrate two clearly different solar-wind streams. From the MVA across 10:37 – 10:49 UT on 28 December 2011 at STA, we find the normal direction of the stream interface is $0.121\hat{\boldsymbol{R}} - 0.370\hat{\boldsymbol{T}} + 0.921\hat{\boldsymbol{N}}$. It is $0.039\hat{\boldsymbol{R}} + 0.902\hat{\boldsymbol{T}} + 0.430\hat{\boldsymbol{N}}$ at STB using the MVA across 14:11 – 14:37 UT on 7 January 2012. At STA, the normal of the stream interface is more aligned with the radial direction; thus the stream interface itself is more tilted to the solar-wind flow, consistent with stronger compression there.

There are four different couplings of photospheric magnetograms and the MHD-Algorithm-outside-a-Sphere (MAS) coronal and heliospheric model (*e.g.* Riley *et al.*, 2011; Lionello *et al.*, 2014) provided for the relevant Carrington rotations by Predictive Science Inc. www.predsci.com/stereo/. The predicted start time of the short magnetic-field sector at STB associated with a small equatorial coronal hole differs by two to three days from observation, and the models capture the short nature of the sector. For STA, all of the sim-

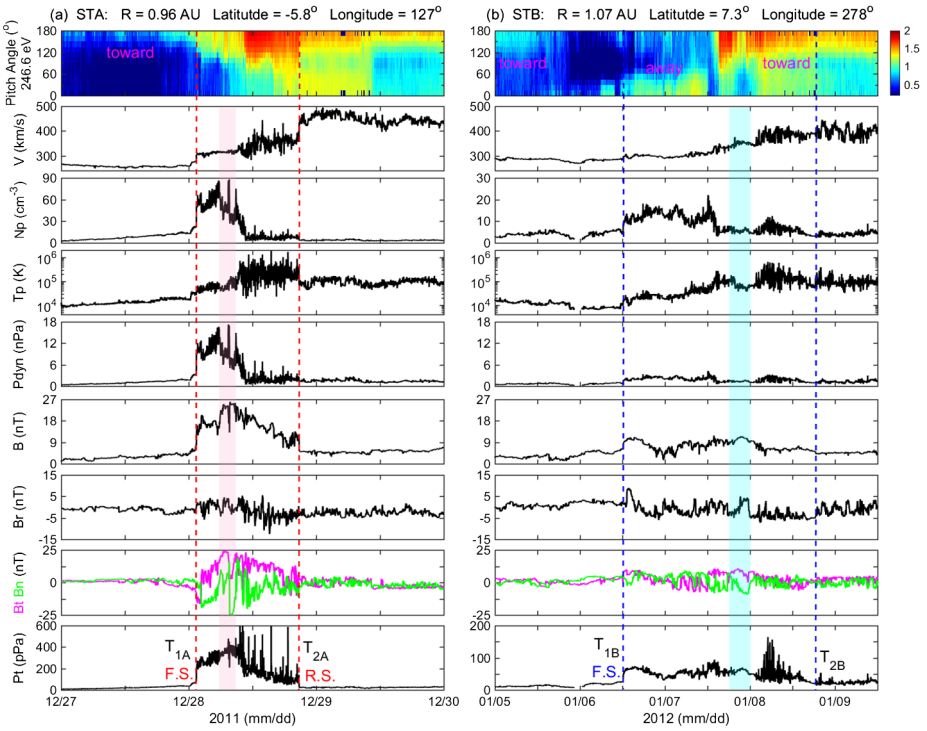

Figure 15 One example of dual observations of SIRs at (**a**) STA and (**b**) STB. From *top* to *bottom*: the pitch-angle distribution of suprathermal-electron flux at 246.6 eV (toward and away sectors are marked), solar-wind speed, proton number density, proton temperature, dynamic pressure, magnetic-field intensity, magnetic-field vector in RTN coordinates, total pressure. The time scale is set differently between (**a**) and (**b**) in order to show the change of magnetic sector at STB. The scales for N_p and P_t differ between (**a**) and (**b**) to better show the compression region. The *red- and blue-dashed lines* mark the boundaries of SIR at STA and STB, respectively. There is a pair of forward–reverse shocks at the edges of the SIR at STA, and only a forward shock is driven by the SIR at STB. The *pink* (*cyan*)*-shaded region* marks the interesting flux rope at STA (STB).

ulation runs predict a small low-latitude coronal hole and an HCS crossing. It is possible that STA flew just above or below the HCS and missed the HCS crossing by chance, which requires multi-point observation in short separation (within SIR scale) to resolve. On the other hand, the modeling input of Carrington-rotation synoptic maps may not present the temporal changes sufficiently. The performance would improve using time-dependent (such as daily) photospheric magnetogram input, although difficulties do exist in implementing such input (Linker *et al.*, 2016). This is especially important near solar maximum in order to provide reliable background solar-wind prediction for CME propagation.

At STA, the magnetic field rotated with large amplitude at 5:30 – 9:00 UT on 28 December 2011, marked by the pink-shaded region, mainly in the tangential and normal directions. There is no bidirectional suprathermal-electron strahl or iron charge-state increase associated with it. Surprisingly, a similar small flux rope occurred at 18:00 – 24:00 UT on 7 January 2012 at STB, marked by the cyan-shaded region. The major field rotation is also in the tangential and normal directions, but the amplitude is much smaller than the one at STA. These two interesting flux ropes occurred near the stream interface, one in the slow-wind side, and the other in the fast-wind side, when the twin spacecraft are nearly at the oppo-

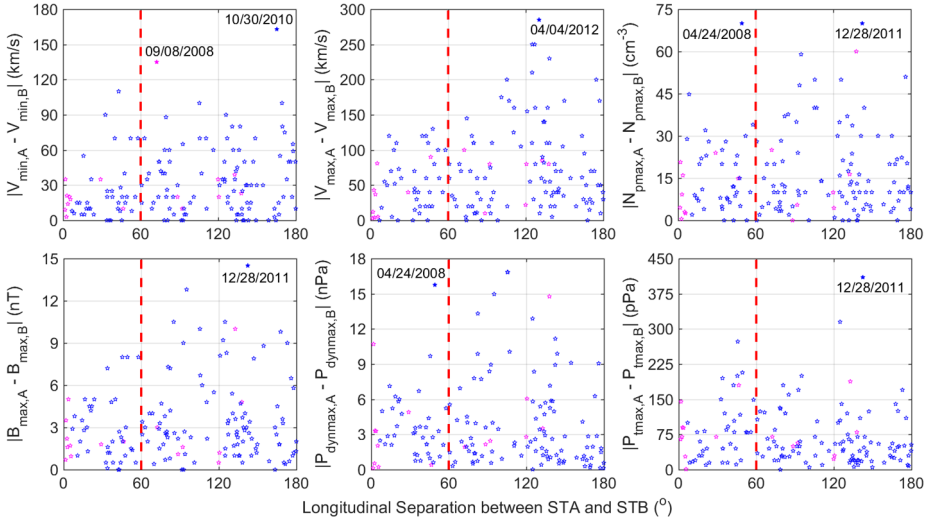

Figure 16 The scatter plots of six SIR parameters: $V_{\rm min}$, $V_{\rm max}$, $N_{\rm pmax}$, $B_{\rm max}$, $P_{\rm dynmax}$, and $P_{\rm tmax}$. The *abscissa* is the smaller longitudinal difference [$\Delta\varphi$] between STA and STB in the range of 0° – 180°, and the *vertical axis* is the absolute difference of parameter values between STA and STB. The *magenta stars* indicate the cases when the absolute $\Delta\theta$ of the twin spacecraft is no more than 1°, and the *blue star*s mark the other cases. In each *panel*, the *red-dashed vertical line* marks the longitudinal difference of 60°. Several extreme cases are denoted by the *filled stars* with the dates at STA marked.

site side of the Sun to each other. No corresponding CME modeling is found at the Space Weather Database of Notifications, Knowledge, Information (DONKI: kauai.ccmc.gsfc.nasa.gov/DONKI/). These short field rotations may be related to blobs or blob-like ejecta (*e.g.* Wang *et al.*, 2000; Sheeley *et al.*, 2009; Song *et al.*, 2009). Although the magnetic field in the small flux rope at STA is unusually strong, reaching above 25 nT, the field compression outside the small flux rope is as high as 20 nT and may have enabled further compression of the small flux rope. Detailed investigations incorporating the remote-sensing observations are needed to decipher their sources and relationships with the stream interfaces. The dual observations for this SIR pair demonstrate how the small transients can cause the temporal variability of the relatively quasi-steady structure of solar wind (*e.g.* Kilpua *et al.*, 2009; Rouillard *et al.*, 2010a, 2010b; Yu *et al.*, 2014, 2016).

Figure 16 summarizes the absolute changes of SIR parameters with the smaller longitudinal separation between STA and STB in the range of 0° – 180°. Corresponding to the increase of $\Delta\varphi$ from 0 to 180°, the time offset increases from 0 to about 15 days at a similar pace (Figure 9). The magenta stars indicate the cases when the latitudes of STA and STB differ by at most 1°. The magenta stars at small $\Delta\varphi$ demonstrate the variability of these SIR parameters in the first few months of the mission. Generally, the parameter discrepancy is greater when the twin spacecraft are farther apart in longitude, regardless of $\Delta\theta$. For a L_4/L_5 mission located 60° apart from the Earth marked by the red-dashed line, the fast-solar-wind speed can differ by up to 100 km s^{-1}; the $B_{\rm max}$ can differ by up to 8 nT; and the $P_{\rm dynmax}$ can differ by up to 16 nPa from L_1 measurement for SIRs. Due to the rapid motion of the STEREO spacecraft, there are only 11 SIR pairs with $\Delta\varphi$ between 50° – 70°. Their median absolute differences of $V_{\rm max}$, $N_{\rm pmax}$, $B_{\rm max}$, $P_{\rm dynmax}$, and $P_{\rm tmax}$ between the dual observations are 60 km s^{-1}, 10 cm^{-3}, 2.5 nT, 2.4 nPa, and 80 pPa, respectively. These values indicate typi-

cal differences between L_4/L_5 measurement and near-Earth observations expected based on this sampled period of time.

6. Summary and Discussion

In the first decade of the mission, the STEREO spacecraft have observed 575 SIRs: 318 by STA in February 2007 – December 2016 and 257 by STB in March 2007 – September 2014. About 8.7% of them are hybrid events interacting closely with ICMEs. In a small number of questionable events, the fast-wind speed is only about 400 – 430 $\mathrm{km\,s^{-1}}$ while two clearly different solar-wind streams are observed. Further systematic investigation on such cases and their solar origins will be conducted in a separate study.

The acceleration rate of the solar-wind speed across SIRs ranges from 0.3 to 8.2 $\mathrm{m\,s^{-2}}$, and the compression of N_p, B, and P_t are all positively correlated with the acceleration. About 33% of SIRs drive shocks, specifically about 19% with only forward shocks, 10% with only reverse shocks, and 4% with forward-reverse shock pairs. The forward-shock rate has a stronger solar-cycle dependence than the reverse-shock rate. In 2009 – 2011 and 2016, the rates of these two types of shocks are similar and at about 10%.

Among 518 well-defined or pristine SIRs, 54% are associated with a clear HCS crossing within three days of stream interface, 34% without any HCS crossing. Their solar origins are related to helmet streamers and pseudo-streamers, respectively. The remaining 12% of SIRs often occur with magnetic sectors shorter than three days. The shock rate of SIRs with HCS is 30%, slightly higher than the rate of 27% for the SIRs without HCS. In comparison with SIRs without an HCS, the SIRs with an HCS generally have slightly slower V_min and V_max but higher N_pmax, B_max, P_tmax, and P_dynmax. The dense HPS and higher occurrence of blobs at streamer belts could be two factors contributing to higher N_pmax. The $\langle Q_\mathrm{Fe}\rangle$ decreases sharply at stream interface, and it is higher on the slow-wind side than on the fast-wind side. The $\langle Q_\mathrm{Fe}\rangle$ is higher throughout SIRs with HCS than SIRs without HCS, by about 1/3 of a charge unit at most, with a two-day increase in the slow-wind side perhaps associated with helmet streamers.

The annual SIR numbers at the twin STEREO spacecraft can significantly differ from each other, by more than ten events in some years. Thus, the dual observations certainly help to build better statistics for Solar Cycle 24. In addition, the subtle difference of SIR properties between STA and STB, as shown in Figure 12 and Table 3, justifies the solar-cycle comparison combining *Wind*/ACE and STEREO observations. In contrast with comparable phases of Solar Cycle 23, there are slightly more SIRs and a higher recurrence rate in Cycle 24, possibly because of the persistent equatorial coronal holes as well as weaker CMEs in this cycle. The HCS association rate of SIRs is 49% in Cycle 24, noticeably lower than 57% in the previous cycle, suggesting that more pseudo-streamers exist in this cycle, in agreement with some analyses based on coronal field geometry (*e.g.* Owens, Crooker, and Lockwood, 2014)

The V_min, V_max, B_max, P_tmax, and P_dynmax of SIRs are all lower in Cycle 24 than in the previous one. The decrease fractions of these parameters are slightly less than the decrease fractions of the general solar-wind except for V_min, indicating that the SIRs weaken less than the background solar wind, similar to the situation for ICMEs found by Jian *et al.* (2018). The SIRs generally last longer, implying wider spatial extent in Cycle 24 than in Cycle 23. In addition, the shock rate of 32% in Cycle 24 is higher than the 25% in the previous cycle, partly due to the slower magnetosonic speed in the background solar wind during this cycle.

Before STB lost contact, 151 SIR pairs (2/3 of the pristine SIRs) were observed by the twin spacecraft with the expected and observed middle time differing by up to three days. The N_{pmax} and P_{dynmax} are somewhat lower at STB than at STA, because of the 0.02 – 0.14 AU difference in heliocentric distance. However, other parameters and shock rates are similar at the two spacecraft. The parameter discrepancy changes widely with latitudinal and longitudinal separation between the twin spacecraft, even within 5° for latitudinal separation and 60° for longitudinal difference, demonstrating the variability of SIRs. Although they are quasi-steady solar-wind structures, SIRs are highly structured with many examples of discontinuities, such as shocks, stream interfaces, and rotational and tangential discontinuities. Furthermore, unlike energetic CMEs, SIRs can more easily be influenced by the background solar wind. Through two examples of dual observations, we have also shown the change of relative location with respect to the HCS, and that the small flux ropes embedded within SIRs can also add to the variability. In these two instances, higher compression at SIRs is not always associated with a higher tilt of the stream interface to the solar-wind flow. The fast-wind speed difference in the SIR pair may have caused the inconsistency. More statistics are needed in future studies to verify whether a higher tilt causes stronger compression when other solar-wind properties are similar.

An SIR typically lasts about 1.5 days at 1 AU, corresponding to about 20° in longitude. To observe the different parts of an SIR simultaneously and understand its three-dimensional structures, we will need mesoscale multi-point observations within the SIR scale, similar to the case for CMEs (Lugaz *et al.*, 2018). In addition, time-dependent photospheric magnetograms (*e.g.* Arge *et al.*, 2010, 2013) and more sophisticated coronal and heliospheric models (*e.g.* Merkin *et al.*, 2016; MacNeice *et al.*, 2018) will help in making progress to resolve the complexity in SIR structures.

Acknowledgements L.K. Jian is supported by NASA's Science Mission Directorate as part of the STEREO project, NASA's Living with a Star and Heliophysics Supporting Research programs. L.K. Jian thanks P. Démoulin, N. Lugaz, and X. Zhou for the helpful discussions. C.T. Russell and J.G. Luhmann appreciate the support of NASA grant NNX15AG09G for IMPACT investigation. A.B. Galvin is supported by NASA grants NNX15AU01G and 80NSSC17K0556 for PLASTIC investigation. We are grateful to the STEREO mission team and NASA's Space Physics Data Facility for providing the data needed for this study.

Disclosure of Potential Conflicts of Interest The authors declare that they have no conflicts of interest.

References

Arge, C., Henney, C., Koller, J., Compeau, C., Young, S., MacKenzie, D., Fay, J., Harvey, A.: 2010, In: Maksimovic, M., Issautier, K., Meyer-Vernet, N., Moncuquet, M., Pantellini, F. (eds.) *Twelfth Int. Solar Wind Conf.* **CP-1216**, AIP, Melville, 343. DOI.

Arge, C.N., Henney, C.J., Gonzalez-Hernandez, I., Toussaint, W.A., Koller, J., Godinez, H.C.: 2013, In: Zank, G.P., Borovsky, J., Bruno, R., Cirtain, J., Cranmer, S., Elliott, H., *et al.* (eds.) *Solar Wind 13: Proc. 13th Int. Solar Wind Conf.*, **CS-1539**, AIP, Melville, 11. DOI.

Bavassano, B., Woo, R., Bruno, R.: 1997, *Geophys. Res. Lett.* **24**, 1655. DOI.

Belcher, J.W., Davis, L. Jr.: 1971, *J. Geophys. Res.* **76**, 3534. DOI.

Borovsky, J.E., Denton, M.H.: 2013, *J. Geophys. Res.* **118**, 5506. DOI.

Chi, Y., Shen, C., Wang, Y., Xu, M., Ye, P., Wang, S.: 2016, *Solar Phys.* **291**, 2419. DOI.

Crooker, N.U., McPherron, R.L., Owens, M.J.: 2014, *J. Geophys. Res.* **119**, 4157. DOI.

Crooker, N.U., Huang, C.-L., Lamassa, S.M., Larson, D.E., Kahler, S.W., Spence, H.E.: 2004a, *J. Geophys. Res.* **109**, A03107. DOI.

Crooker, N.U., Kahler, S.W., Larson, D.E., Lin, R.P.: 2004b, *J. Geophys. Res.* **109**, A03108. DOI.
Crooker, N.U., Antiochos, S.K., Zhao, X., Neugebauer, M.: 2012, *J. Geophys. Res.* **117**, A04104. DOI.
Feldman, W.C., Asbridge, J.R., Bame, S.J., Fenimore, E.E., Gosling, J.T.: 1981, *J. Geophys. Res.* **86**, 5408. DOI.
Foullon, C., Lavraud, B., Luhmann, J.G., Farrugia, C.J., Retinò, A., Simunac, K.D.C., *et al.*: 2011, *Astrophys. J.* **737**(1), 16. DOI.
Fränz, M., Harper, D.: 2002, *Planet. Space Sci.* **50**(2), 217. DOI.
Galvin, A.B., Kistler, L.M., Popecki, M.A., Farrugia, C.J., Simunac, K.D.C., Ellis, L., *et al.*: 2008, *Space Sci. Rev.* **136**, 437. DOI.
Galvin, A.B., Popecki, M.A., Simunac, K.D.C., Kistler, L.M., Ellis, L., Barry, J., *et al.*: 2009, *Ann. Geophys.* **27**, 3909. DOI.
Gómez-Herrero, R., Klassen, A., Müller-Mellin, R., Heber, B., Wimmer-Schweingruber, R., Böttcher, S.: 2009, *J. Geophys. Res.* **114**, A05101. DOI.
Gosling, J.T., Pizzo, V.J.: 1999, *Space Sci. Rev.* **89**, 21. DOI.
Gosling, J.T., Asbridge, J.R., Bame, S.J., Feldman, W.C.: 1978, *J. Geophys. Res.* **83**, 1401. DOI.
Gosling, J.T., Borrini, G., Asbridge, J.R., Bame, S.J., Feldman, W.C., Hansen, R.T.: 1981, *J. Geophys. Res.* **86**, 5438. DOI.
Gosling, J.T., McComas, D.J., Skoug, R.M., Forsyth, R.J.: 2001, *Space Sci. Rev.* **97**, 189. DOI.
Harvey, J.W., Hill, F., Hubbard, R.P., Kennedy, J.R., Leibacher, J.W., Pintar, J.A., Gilman, P.A., *et al.*: 1996, *Science* **272**(5266), 1284. DOI.
Heinemann, S.G., Temmer, M., Hofmeister, S.J., Veronig, A.M., Vennerstrøm, S.: 2018, *Astrophys. J.* **861**, 151. DOI.
Jian, L.: 2008, Radial evolution of large-scale solar wind structures. Ph.D. Thesis, UCLA.
Jian, L.K., Russell, C.T., Luhmann, J.G.: 2011, *Solar Phys.* **274**, 321. DOI.
Jian, L., Russell, C.T., Gosling, J.T., Luhmann, J.G.: 2005, In: Fleck, B., Zurbuchen, T.H., Lacoste, H. (eds.) *Proc. Solar Wind 11-SOHO 16, Connecting Sun and Heliosphere*, **SP-592**, ESA, Noordwijk, 491.
Jian, L., Russell, C.T., Luhmann, J.G., Skoug, R.M.: 2006a, *Solar Phys.* **239**, 337. DOI.
Jian, L., Russell, C.T., Luhmann, J.G., Skoug, R.M.: 2006b, *Solar Phys.* **239**, 393. DOI.
Jian, L.K., Russell, C.T., Luhmann, J.G., Skoug, R.M., Steinberg, J.T.: 2008a, *Solar Phys.* **249**, 85. DOI.
Jian, L.K., Russell, C.T., Luhmann, J.G., Skoug, R.M.: 2008b, *Adv. Space Res.* **41**, 259. DOI.
Jian, L.K., Russell, C.T., Luhmann, J.G., Skoug, R.M., Steinberg, J.T.: 2008c, *Solar Phys.* **250**, 375. DOI.
Jian, L.K., Russell, C.T., Luhmann, J.G., Galvin, A.B., MacNeice, P.J.: 2009, *Solar Phys.* **259**, 345. DOI.
Jian, L.K., Russell, C.T., Luhmann, J.G., MacNeice, P.J., Odstrcil, D., Riley, P., Linker, J.A., Skoug, R.M., Steinberg, J.T.: 2011, *Solar Phys.* **273**, 179. DOI.
Jian, L.K., Russell, C.T., Luhmann, J.G., Galvin, A.B., Simunac, K.D.C.: 2013, In: Zank, G.P., Borovsky, J., Bruno, R., Cirtain, J., Cranmer, S., Elliott, H., *et al.* (eds.) *Solar Wind 13: Proc. 13th Int. Solar Wind Conf.*, **CS-1539**, AIP, Melville, 191. DOI
Jian, L.K., MacNeice, P.J., Taktakishvili, A., Odstrcil, D., Jackson, B., Yu, H.-S., *et al.*: 2015, *Space Weather* **13**, 316. DOI.
Jian, L.K., MacNeice, P.J., Mays, M.L., Taktakishvili, A., Odstrcil, D., Jackson, B., *et al.*: 2016, *Space Weather* **14**, 592. DOI.
Jian, L.K., Russell, C.T., Luhmann, J.G., Galvin, A.B.: 2018, *Astrophys. J.* **855**, 114. DOI.
Kaiser, M.L., Kucera, T.A., Davila, J.M., St. Cyr, O.C., Guhathakurta, M., Christian, E.: 2008, *Space Sci. Rev.* **136**, 5. DOI.
Kilpua, E.K.J., Luhmann, J.G., Gosling, J., Li, Y., Elliott, H., Russell, C.T., *et al.*: 2009, *Solar Phys.* **256**, 327. DOI.
King, J.H., Papitashvili, N.E.: 2005, *J. Geophys. Res.* **110**, A02104. DOI.
Leibacher, J.W.: 1999, *Adv. Space Res.* **24**, 173. DOI.
Linker, J.A., Caplan, R.M., Downs, C., Lionello, R., Riley, P., Mikic, Z., *et al.*: 2016, *J. Phys.* **CS-719**, 012012. DOI.
Lionello, R., Velli, M., Downs, C., Linker, J.A., Mikic, Z., Verdini, A.: 2014, *Astrophys. J.* **784**, 120. DOI.
Lugaz, N., Farrugia, C.J., Winslow, R.M., Al-Haddad, N., Galvin, A.B., Nieves-Chinchilla, T., Lee, C.O., Janvier, M.: 2018, *Astrophys. J. Lett.* **864**, L7. DOI.
Luhmann, J.G., Curtis, D.W., Schroeder, P., McCauley, J., Lin, R.P., Larson, D.E., *et al.*: 2008, *Space Sci. Rev.* **136**, 117. DOI.
MacNeice, P., Jian, L.K., Antiochos, S.K., Arge, C.N., Bussy-Virat, C.D., DeRosa, M.L., *et al.*: 2018, *Space Weather* **16**, 1644. DOI.
McComas, D.J., Riley, P., Gosling, J.T., Balogh, A., Forsyth, R.: 1998, *J. Geophys. Res.* **103**, 1955. DOI.
Merkin, V.G., Lyon, J.G., Lario, D., Arge, C.N., Henney, C.J.: 2016, *J. Geophys. Res.* **121**, 2866. DOI.
Neugebauer, M., Liewer, P.C., Goldstein, B.E., Zhou, X., Steinberg, J.T.: 2004, *J. Geophys. Res.* **109**, A10102. DOI.

Newton, H.W., Nunn, M.L.: 1951, *Mon. Not. Roy. Astron. Soc.* **111**, 413. DOI.
Opitz, A., Karrer, R., Wurz, P., Galvin, A.B., Bochsler, P., Blush, L.M., *et al.*: 2009, *Solar Phys.* **256**, 365. DOI.
Owens, M.J., Crooker, N.U., Lockwood, M.: 2013, *J. Geophys. Res.* **118**, 1868. DOI.
Owens, M.J., Crooker, N.U., Lockwood, M.: 2014, *J. Geophys. Res.* **119**, 36. DOI.
Richardson, I.G., Mazur, J.E., Mason, G.M.: 1998, *J. Geophys. Res.* **103**(A2), 2115. DOI.
Riley, P., Lionello, R., Linker, J.A., Mikic, Z., Luhmann, J., Wijaya, J.: 2011, *Solar Phys.* **274**, 361. DOI.
Roberts, D.A., Thieman, J., Génot, V., King, T., Gangloff, M., Perry, C., *et al.*: 2018, *Space Weather* **16**, 1899. DOI.
Rouillard, A.P., Davies, J.A., Lavraud, B., Forsyth, R.J., Savani, N.P., Bewsher, D., *et al.*: 2010a, *J. Geophys. Res.* **115**, A04103. DOI.
Rouillard, A.P., Lavraud, B., Davies, J.A., Savani, N.P., Burlaga, L.F., Forsyth, R.J., *et al.*: 2010b, *J. Geophys. Res.* **115**, A04104. DOI.
Russell, C.T., Shinde, A.A., Jian, L.: 2005, *Adv. Space Res.* **35**, 2178. DOI.
Sheeley, N.R. Jr., Lee, D.D.-H., Casto, K.P., Wang, Y.-M., Rich, N.B.: 2009, *Astrophys. J.* **94**, 1471. DOI.
Simunac, K.D.C., Kistler, L.M., Galvin, A.B., Lee, M.A., Popecki, M.A., Farrugia, C., *et al.*: 2009, *Solar Phys.* **259**, 323. DOI.
Song, H.Q., Chen, Y., Liu, K., Feng, S.W., Xia, L.D.: 2009, *Solar Phys.* **258**, 129. DOI.
Sonnerup, B.U.O., Cahill, L.J.: 1967, *J. Geophys. Res.* **72**, 171. DOI.
Temmer, M., Rybák, J., Bendík, P., Veronig, A., Vogler, F., Otruba, W., Pötzi, W., Hanslmeier, A.: 2006, *Astron. Astrophys.* **447**, 735. DOI.
van Hollebeke, M.A.I., McDonald, F.B., Trainor, J.H., von Rosenvinge, T.T.: 1978, *J. Geophys. Res.* **83**, 4723. DOI.
Wang, Y.-M., Sheeley N.R. Jr., Rich, N.B.: 2007, *Astrophys. J.* **658**, 1340. DOI.
Wang, Y.-M., Sheeley N.R. Jr., Socker, D.G., Howard, R.A., Rich, N.B.: 2000, *J. Geophys. Res.* **105**, 25133. DOI.
Wang, Y.-M., Grappin, R., Robbecht, E., Sheeley, N.R.: 2012, *Astrophys. J.* **749**, 182. DOI.
Winterhalter, D., Smith, E.J., Burton, M.E., Murphy, N., McComas, D.J.: 1994, *J. Geophys. Res.* **99**, 6667. DOI.
Yu, W., Farrugia, C.J., Lugaz, N., Galvin, A.B., Kilpua, E.K.J., Kucharek, H., *et al.*: 2014, *J. Geophys. Res.* **119**, 689. DOI.
Yu, W., Farrugia, C.J., Galvin, A.B., Lugaz, N., Luhmann, J.G., Simunac, K.D.C., Kilpua, E.: 2016, *J. Geophys. Res.* **121**, 5005. DOI.
Zhao, L., Landi, E., Lepri, S.T., Gilbert, J.A., Zurbuchen, T.H., Fisk, L.A., Raines, J.M.: 2017, *Astrophys. J.* **846**, 135. DOI.